Single-Stranded Adenine-Rich DNA and RNA Retain Structural Characteristics of Their Respective Double-Stranded Conformations and Show Directional Differences in Stacking Pattern†

J. Isaksson, S. Acharya, J. Barman, P. Cheruku, and J. Chattopadhyaya*

Department of Bioorganic Chemistry, Box 581, Biomedical Center, Uppsala University, S-751 23 Uppsala, Sweden

Received August 17, 2004; Revised Manuscript Received October 7, 2004

ABSTRACT: The structural preorganization of isosequential ssDNA and ssRNA hexamers d/r(GAAAAC)$_1$ [*J. Am. Chem. Soc.* **2003**, *125*, 9948] have been investigated by NMR and molecular dynamics simulations. Analysis of the nuclear Overhauser effect spectrometry (NOESY) footprints in the aqueous solution has shown that there is a substantial population of ordered right-handed helical structure in both hexameric single-stranded DNA and RNA, which are reminiscent of their respective right-handed helical duplex form, despite the fact these single-stranded molecules are devoid of any intermolecular hydrogen bonds. The NMR-constrained molecular dynamics (1.5 ns) derived geometries of the adenine−adenine overlaps at each dinucleotide step of the hexameric ssDNA (**1a**) and ssRNA (**1b**) show that the relatively electron-rich imidazole stacks above the electron-deficient pyrimidine in 5′ to 3′ direction in ssDNA (**1a**) while, in contradistinction, the pyrimidine stacks above the imidazole in the 5′ to 3′ direction in ssRNA (**1b**). This also means that the π-frame of the 5′-pyrimidine can interact with the relatively positively charged imino and amino protons in the 3′ direction in ssRNA and in the 5′ direction in ssDNA, thereby stabilizing the twist and slide observed in the stacked oligonucleotides. The differently preferred stacking geometries in ssDNA and ssRNA have direct physicochemical implications for self-assembly and pK_a modulation by the nearest-neighbor interactions, as well as for the dangling-end stabilization effects and imino-proton reactivity.

In single-stranded (ss) DNA and RNA, the helix is devoid of intermolecular hydrogen bonding, which normally helps to stabilize the double-stranded form (*1a*,*b*). In ssRNA, the self-assembly is further stabilized by the presence of the 2′-OH group, as well as by both canonical and noncanonical hydrogen bonds, stacking, and metal ion interactions to give complex biologically vital RNA scaffolds. Although much is known about the role of stacking in dictating the geometry and function of single-stranded nucleic acids, in general (*2*, *3*), by low-resolution NMR (*3a*−*c*,*i*,*j*), calorimetry (*4d*), absorption spectroscopy (*3k*), optical rotatory dispersion (ORD) (*3h*), or osmometry (*3g*), no direct high-field NMR studies on the stacking interaction patterns have yet been available on sequences that do not form any higher order conformations such as hairpins or pseudoknots. Although there are several reports of high-resolution structures of ssDNA and ssRNA bound to various proteins (*4b*,*m*,*o*−*s*), they reveal very little about the structural preferences of the unbound oligomers since a common feature upon protein binding is that the protein retains most of its structural integrity while the oligomers undergo an induced fit upon binding. On the other hand, some recent papers have shed considerable light regarding the nature of intramolecular aromatic interactions in nucleic acids and their complexes (*4*, *5*) by critical analysis of X-ray crystallographic data.

Many ssDNAs and ssRNAs show their functional properties upon binding to specific proteins (*2*, *4*). Specific recognition of single-stranded nucleic acids is a fundamental requirement in the most central biological processes (*4j*) such as telomere recognition, DNA replication and repair, transcription, translation, and RNA processing. It is also well established that single-stranded dangling ends add to the stability of both DNA and RNA duplexes (*6*). Comparison of ssDNA with ssRNA dangling-end motifs shows (*6c*) that 5′-dangling ends on a DNA/DNA duplex contribute to its stability equally or more than their RNA counterparts. Conversely, 3′-dangling ends on a RNA/RNA duplex (*6a*,*e*) contribute to stability equally or more than their DNA counterparts (*6c*).

Vesnaver and Breslauer have shown by differential scanning calorimetry that a 13mer ssDNA has some ordered single-stranded structure (*4d*). An in-depth understanding of the preorganized conformations of ssDNA and ssRNA is a prerequisite to understand various intra- and intermolecular associations of nucleic acids, as well as to engineer improved hybridization probes to form homo- or heteroduplexes and -triplexes having diagnostic, catalytic, or therapeutic potential and prebiotic chemistry implications (*2*, *7*).

pH-dependent NMR and biochemical reactivity studies (*8*) have shown that local changes in the microenvironment cause

† Generous financial support from the Swedish Natural Science Research Council (Vetenskapsrådet), Stiftelsen för Strategisk Forskning, and Philip Morris, U.S.A., Inc., is gratefully acknowledged.

* To whom correspondence should be addressed. E-mail: jyoti@boc.uu.se. Phone: +46 18 4714577. Fax: +46 18 554495.

10.1021/bi048221v CCC: $27.50
Published on Web 11/25/2004

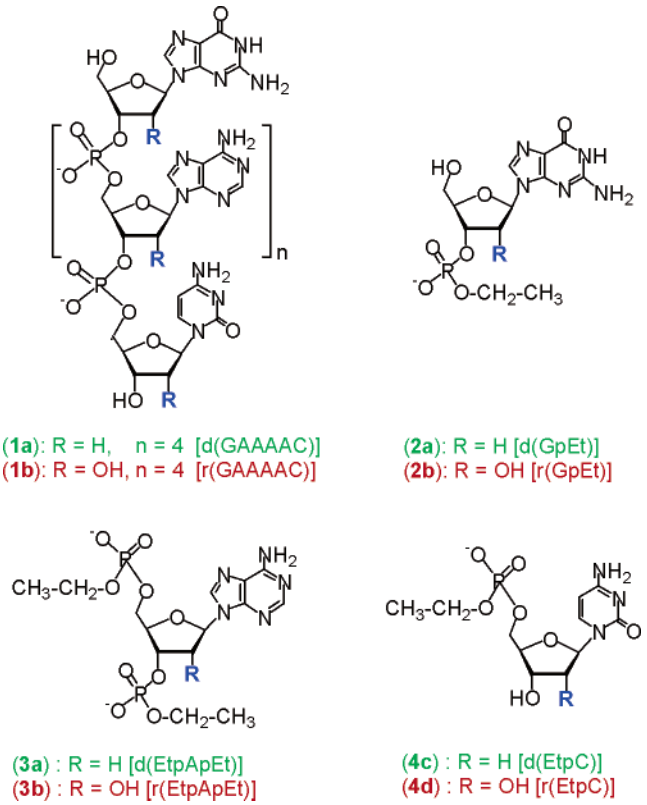

FIGURE 1: The molecular structures of the studied (5′-GAAAAC-3′)$_1$ hexamers (**1a** and **1b**), as well as the blocks used for calculations of oligomerization shifts (**2a**, **2b**, **3a**, **3b**, **4a**, and **4b**).

a large number of RNA, and in some cases DNA, to have their pK_a values of their protonation/deprotonation sites significantly perturbed relative to the pK_a of the corresponding monomer. The pK_a perturbation of the aglycone in DNA or RNA is most likely the result of restricted accessibility of the aqueous environment to the immediate proximity of the protonation/deprotonation site. Such shifts in pK_a values of aglycones in DNA and RNA have recently been recognized (*7*, *8*) to be an important source of information about neighboring electrostatics, as well as the partial charge distribution over the whole molecule, which are useful to understand the modulation of the chemical reactivity and functional specificity.

In the present study, two hexamers, d(GAAAAC)$_1$ (**1a**) and r(GAAAAC)$_1$ (**1b**) (Figure 1), were chosen as model systems since extensive pH- and temperature-dependent NMR data (*7f*, Table S3 in the Supporting Information) were already available for these two compounds and they showed different pK_a modulation in ssRNA in relation to ssDNA (Table S3 in the Supporting Information), which strongly hinted that their nearest-neighbor adenine−adenine stacking interactions are different.

We here report our NMR studies of the structures of hexameric ssDNA (**1a**) and ssRNA (**1b**) determined using NMR-constrained molecular dynamics simulations, both at constant temperature and by a temperature cycling protocol. The hexamers both adopt a dominant conformation in the aqueous solution in the NMR time scale that is reminiscent of the B-type helix for the ssDNA hexamer (**1a**) and of A-type helix for the ssRNA hexamer (**1b**).

EXPERIMENTAL PROCEDURES

A. NMR Experiments. All NMR experiments (*7*) were performed on a DRX-600 spectrometer. The protons of all compounds have been assigned by ^{1}H nuclear Overhauser effect spectrometry (NOESY), ^{1}H double-quantum-filtered correlation spectroscopy (DQF-COSY) with and without ^{31}P decoupling and ^{31}P,^{1}H correlation spectroscopy at 278, 283, and 298 K. All NOESY spectra were recorded using a mixing time (τ_m) of 500 and 800 ms. For each free induction decay (FID) of NOESY, ^{1}H DQF-COSY, ^{31}P-decoupled ^{1}H DQF-COSY, and total correlation spectroscopy (TOCSY) spectrum, 64−128 scans were recorded with a relaxation delay of 2 s. Four thousand complex data points were collected in the t_2 dimension, and 256−1024 experiments were run in the t_1 dimension.

B. Assignment. The assignments of dGAAAAC (**1a**) and rGAAAAC (**1b**) are presented in Figure S1, panels A−G, in the Supporting Information. All chemical shifts are given in Table S4 in the Supporting Information.

C. NMR-Constrained Molecular Dynamics Simulations. (i) Structure Building. Canonical starting structures for the hexameric ssDNA and ssRNA were built with SYBYL (*9*) using the biopolymer option. The DNA hexamer was built from a B-type antiparallel duplex (because of the observed typical B-type NOESY footprint), where the second strand was subsequently deleted. The RNA hexamer was built (because of the observed typical A-type NOESY footprint) correspondingly from an A-type antiparallel RNA duplex, where the second strand was deleted. The XLEAP module configured with the parm94 parameter set for AMBER 6.0 (*10*) was used to create the topology file and final starting coordinates. The ssDNA was solvated in a periodic box with the dimensions 41 × 45 × 47 Å^3 filled with 2001 TIP3P water molecules, surrounding the molecule by 10 Å in all dimensions. With the same procedure, the ssRNA was solvated in a 41 × 46 × 46 Å^3 box filled with 2009 water molecules. The phosphate negative charges were neutralized by the addition of Na^+ counterions, replacing nearby overlapping water molecules.

(ii) NMR Constraints Used for the Molecular Dynamics Simulations. The $\sum_{H1'}$ and $\sum_{H2'}$ sums of couplings from the phosphorus decoupled DQF-COSY were used to estimate the percent of 2′-*endo* and 3′-*endo* sugar conformations (*11*) of all residues of both the DNA and the RNA hexamers (Table 1). The ssDNA residues G, A^1, A^2, A^3, and A^4 were found to be predominantly (75%) in South-type conformation and were constrained to $P = 120-210°$, and the ssRNA A^2, A^3, A^4, and C residues, which were found to be predominantly (>75%) in North-type conformation, were constrained to $P = 0-120°$. The ssDNA G^1 and ssRNA G^1 and A^1 residues showed mixed conformations (<75% of either 2′-*endo* or 3′-*endo*) and were constrained to $P = 0-210°$.

Qualitative NMR data was used to draw conclusions (*12*−*15*) about the available conformational hyperspace of the backbone. The (*n*)P−(*n*)H4′ correlation is only detectable when the four bonds in the H4′−C4′−C5′−O5′−P backbone are located in the same plane forming a W-shaped conformation (*15*). This is possible when the β and γ torsions are trans and gauche$^+$, respectively, which is the most common conformation for both A- and B-DNA. The presence of strong (*n*)P−(*n*)H4′ cross-peaks for all residues for both

Table 1: The $\Sigma^3J_{H1'}$ (in Hz) of the Sugar Moiety in Each Nucleotide by ^{1}H NMR at 298 K

	$\Sigma J_{H1'}$ (Hz)						population of North-type[a] conformers (%)					
ssDNA/ssRNA	G	A^1	A^2	A^3	A^4	C	G	A^1	A^2	A^3	A^4	C
d($GA^1A^2A^3A^4C$)	14.8	13.9	15.5	15.0	14.4	13.5	15	31	3	12	22	37
r($GA^1A^2A^3A^4C$)	4.8	3.5	2.1	2.0	2.1	2.7	45	63	84	86	84	75

[a] DNA, %N = 100(1 − ($\Sigma J_{H1'}$ − 9.8)/5.9) (*11a*); RNA, %N = 100(7.9 − $^3J_{1'2'}$)/6.9 (*11b*).

ssDNA and ssRNA shows that the β^t and γ^+ conformations are frequently populated.

The $^3J_{H4'H5''}$ coupling is very sensitive to the γ torsion (*11*, *12*). When the γ torsion is in gauche$^+$ conformation, there will be no strong couplings between H4′ and any of the H5's (1.0−2.5 Hz) while both trans and gauche$^-$ will result in a strong (∼10 Hz) coupling between the H4′ and one of the H5's. No strong $^3J_{H4'H5''}$ could be confirmed for any residue for either ssDNA or ssRNA. It should however be noted that this region is severely crowded, especially for RNA.

If ϵ is in gauche$^-$ conformation, it should produce a detectable $^4J_{H2'P}$ coupling when the sugar is in South-type conformation. For ssDNA, no such cross-peaks could be observed; thus the ϵ torsion is dominated by trans conformation (*12*) since gauche$^+$ appears to be sterically forbidden (*1a*). For ssRNA, $^4J_{H2'P}$ cross-peaks were observable for residues G, A^1, A^2, and A^3. Since the sugar conformation of the ssRNA is mainly in 3′-*endo* conformation, only the sterically forbidden ϵ^+ was excluded.

NOESY cross-peaks at 800 ms mixing time were used as loose constraints throughout the molecular dynamics simulation. The cross-peaks were classified as either strong or weak and were assigned to 1.8−5.0 and 3.0−6.5 Å, respectively. Strong peaks are considered to originate from direct dipole−dipole NOE transfer, while the constraints of the weak peaks allow for a large contribution from spin-diffusion during the relatively long mixing time, 800 ms. All interresidue cross-peaks used in the simulation are showed in Figure S3 in the Supporting Information.

(iii) Molecular Dynamics. The system was first equilibrated in several steps. First the solute was restrained, while the water molecules were minimized for 1000 steps using the steepest descent minimization algorithm. This minimization step is then repeated once restraining only the heavy atoms in the solute. Second, a short MD simulation using 1 fs time steps was run on the system, once again with restrained solute, heating from 100 to 298 K during 3 ps and was then simulated for a total of 30 ps to allow the water molecules rearrange and relax. Another 30 ps of MD was run on the water molecules only, introducing long-range electrostatic interactions using particle mesh Ewald summation. Finally, the whole system was minimized in five cycles, 1000 steps each, gradually releasing the restraints on the solute molecule. Before the production run was started, the system was once more heated from 100 to 298 K during the first 3 ps of a 30 ps MD simulation. During the 3 ps of heating, the experimentally derived NMR distance and dihedral constrains were also scaled up from 0 to 20 kcal mol^{-1} Å^{-2} and 0−2 kcal mol^{-1} rad^{-2}, respectively, and kept constant during the rest of the simulation. The productive MD was then run using 1.5 fs time steps, 9.0 Å VdW interactions cutoff, and the particle mesh Ewald summation method with 1.0 dielectric constant for the long-range electrostatic interactions. The root-mean-square deviation (RMSD) and energy profile of the trajectory was monitored, and the simulation was stopped when both variables had reached equilibrium at 298 K. The MD simulations for both ssDNA and ssRNA were run for 1.5 ns, followed by 1.5 ns of unconstrained simulation.

(iv) Simulated Annealing (SA) MD Simulations. All simulations were performed solvated in a box filled with water molecules with added sodium ions. The starting structures (B-type ssRNA and A-type ssDNA) were heated from 100 to 450 K during 10 ps of MD at constant pressure. The MD was then run at 450 K for another 10 ps while gradually increasing the strength of the dihedral and sugar constraints (Table S2 in the Supporting Information) to full strength (50 kcal mol^{-1} rad^{-2}) and softly introducing the NOE constraints (10 kcal mol^{-1} Å^{-2}), as shown in Figure S3 in the Supporting Information (all SA-MD constraints are identical to the constrained MD protocol except the sugar pucker constraints, which were 0−60° for N-type and 150−210° for S-type). The strength of NOE constraints were increased to 50 kcal mol^{-1} Å^{-2}, together with the dihedral constraints (50 kcal mol^{-1} rad^{-2}), while cooling the system to 100 K during another 10 ps MD simulation. This was then cycled to produce 30 structures, saving the coordinates each time the low temperature was reached (total protocol for 900 ps), which were further minimized, using 5000 steps of gradient minimization. The structures were accepted on the criteria of total potential energy in vacuo (which were in agreement with the NMR observed sugar conformation, Table 1).

(v) Structure Sampling. MD coordinates were dumped to the trajectory every 0.15 ps of the molecular modeling simulation. From the trajectory, structures were extracted and saved as snapshots every 10 ps from 480 ps and to the end of the simulation at 1.4 ns for the ssDNA simulation and 1.1 ns for the ssRNA simulation. Ten snapshots from the last 100 ps of the simulation were then stripped of water and analyzed for RMSD and total potential energy. The average structure of the MD trajectory of the last 100 ps was also calculated based on one coordinate set per 0.15 ps and minimized for 2000 steps using the conjugate gradient method and the full NMR constraints switched on to bring the most obvious averaging effects back to equilibrium (RMSD between the initial average and the minimized average was <0.3 Å).

(vi) Structure Analysis of the Backbone. The ptraj module for Amber 6.0 was used to extract the dihedrals of the sugar−phosphate backbone and the sugar phase angles from the average structure.

(vii) Structure Analysis of the Helical Parameters. The X3DNA program (*16*) was used to calculate the helical

parameters of the single-stranded DNA and RNA average oligos.

D. Calculations of Shielding Factor. The shielding tensors affecting protons near various aromatic systems have previously been quantified by ab initio calculations with the gauge invariant atomic orbital (GIAO) method (*17*) using the HF/6-31G* theory level (*18*). A common feature of the calculated shielding gradients for benzene and carbonyl model systems is that when moving from the center of the aromatic bond in a plane that lies 3−4 Å above or under (*Z*-axis displacement) the plane of the bond toward any edge the shielding drops sharply from maximum shielding to no shielding at a displacement in the *X*−*Y* plane of approximately 2 Å from the bond.

Based on the theoretical observations above, a model has been used to estimate the combined shielding effect on each base proton (H6/H8 and H2/H5) for the modeled ssRNA and ssDNA. The displacement in the *X*−*Y* plane (Å) of each proton (H8, H2, and H6) from the nearest edge of the neighboring nucleobases was first measured in both the 3′ ($n + 1$) and 5′ ($n - 1$) directions. Each of these distances were then normalized to a sigmoidal function, $y = 1 - 1/\{1 + 10^{[(2-x)/2]}\}$, that has the characteristic that it maintains its maximum value (1.0) and then drops to its minimum value (0.0) at a point centered around an *x*-value of 2 Å, using the scaling factor 0.5. The value for the 3′ ($n + 1$) and 5′ ($n - 1$) directions were then summed to give a total value between 0 and 2 that is proportional to the shielding received from the neighboring ring systems.

This model is based on the approximations that the ring current is evenly distributed in the neighboring nucleobases and that the rise is the same between all adenine steps. Since the structures used in this model only represent a state in which the molecules reside between 50% and 75% of the NMR time, we consider this model sufficiently accurate to show the differences in stacking between ssDNA and ssRNA.

RESULTS

A. Internal Motion and Overall Molecular Tumbling. Compared to the double-stranded forms, the nucleobases in ssDNA and ssRNA have much more motional freedom due to the absence of interstrand hydrogen bond stabilization. Therefore, lower energy barriers of internal motion of both the opening and slide of the nucleobase itself and the pseudorotation of the sugar moieties are expected, resulting in overall increased dynamics. The size of the oligomers studied are relatively small, leading to short correlation times compared to the more commonly studied larger duplex structures. This has a direct effect on the NOE build-up rates (*19*). The increased dynamics can make any specific pair of protons spend more time in conformations that either do contribute very strongly or do not contribute at all to the net NOE transfer, thereby leading to either over- or underestimation of the corresponding distances. Second, the short correlation time of both the overall molecular tumbling and the internal motions will reduce the NOE transfer rate through the spectral density function, resulting in slow build-up rates. With this in mind, NOESY cross-peaks have not been quantified numerically, nor could any full relaxation matrix treatment be performed, because the substantial presence of internal dynamics could lead to overestimations of the corresponding distances (*19*). Instead, the NOESY cross-peaks have been forgivingly classified as strong or weak, where strong cross-peaks correspond to a distance shorter than 5.0 Å and weak cross-peaks correspond to a distance shorter than 6.5 Å. The main conclusions of differences in stacking preorganization in ssDNA and ssRNA are made by comparing the relative intensities of corresponding cross-peaks in ssDNA and ssRNA with respect to each other and classifying them as being stronger or weaker.

B. Single-Strand Stacking. The shielding of aromatic protons as a function of temperature, pH, and concentration has previously been used as a way to roughly quantify the stacking between the stacking adenines (*20*). We here use the crystal structure of the Dickerson−Drew dodecamer (DD) and the corresponding ^{1}H chemical shifts of the aromatic H2 proton as a starting point to define a fully stacked adenine by assuming that in the solution state the DD only exists in duplex form at 273 K. The H2A^5 is completely overlapped by the shielding cone of the A^6 aromatic ring system (Figure 2B), while the H8A^6 proton is extruded into the major groove and therefore is not a useful marker, since it does not provide a value of the maximum shielding in fully stacked form. Compared to the monomeric 2′-deoxyadenosine 3′,5′-bis-ethyl phosphate (**3a**) (Figure 1), the H2A^5 proton in DD experiences a 1.09 ppm upfield shift (O_{oligo}, see section G) due to the stacked conformation in the duplex (note that the H2 proton does not participate directly in interstrand hydrogen bonding). The central H2's of A^2 and A^3 in ssDNA (**1a**) (Figure 1) have corresponding oligomerization shifts of 0.81 and 0.87 ppm (Table 2), thus showing that these protons experience 70−80% of the shielding effect that a stacked H2 proton in a purine tract in a structurally known duplex structure does. The shielding of the same protons has further been compared at 363 K where all specific base−base interactions are assumed to be thermally distorted, and the H2 protons only experience the shielding from random internal motion. The same comparison using the relative deshielding induced by temperature-dependent destacking (273−363 K) instead shows that the H2 protons in ssDNA ($\Delta\delta = 0.39$ and 0.45 ppm) experience 50−60% of the deshielding that the corresponding protons in the duplex melting do ($\Delta\delta = 0.77$) (Table 2). In conclusion, the relative shielding indicates that the central adenine bases in the ssDNA hexamer reside more than 50% of the time in a stacked geometry in aqueous solution at low temperature.

C. ssDNA and ssRNA Backbone Preorganization. In a double-stranded DNA or RNA oligomer, a NOE footprint pattern can provide direct evidence for the helical turn of the molecule. The observed footprint pattern found (Figure 3) for ssDNA and ssRNA suggests that they have right-handed helical structure, which very closely corresponds to those expected (Table 3) for the corresponding double-stranded helix. NOESY spectra showed sequential NOE connectivity between each of the neighboring residues for both ssDNA and ssRNA. In both A- and B-type DNA conformation, the H6/H8$_n$ of one nucleobase to the sugar of the previous residue (H1′, H2′/″, H3′)$_{n-1}$ to its base H6/H8$_{n-1}$ on to the next neighboring sugar residue (H1′, H2′/″, H3′)$_{n-2}$ form a pattern throughout the helix with distances that are between 2.0 and 5.1 Å (all distances for canonical A- and B-type models are shown in Table S1 in the Supporting Information). A typical Z-type structure does not produce

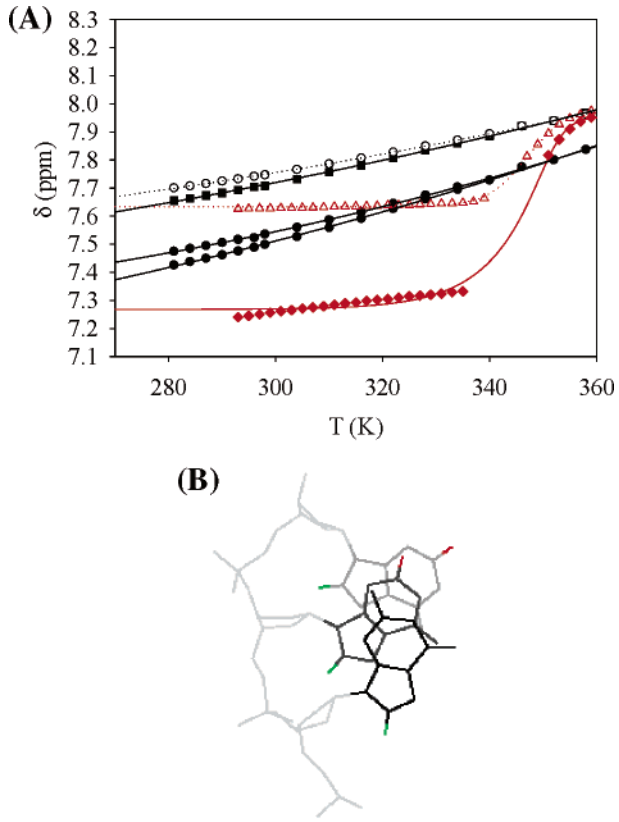

FIGURE 2: Panel A shows a plot of the change in chemical shift (δ) versus temperature (K). Comparison of the shielding of H2A[3] and H2A[4] at 20 °C [black solid circles] to the shielding of H2A[5] in the Dickerson dodecamer [red solid diamonds] (5′-purine-adenine-purine-3′) shows that the single-stranded bases experience roughly 50−60% of the shielding that the double-stranded bases do. For H2A[5] [black open circles] compared with the shielding of H2A[6] in the Dickerson dodecamer [red open triangles] (5′-purine-adenine-pyrimidine-3′), the ratio of experienced shielding is ∼80% for the single-stranded base. The H2A[2] [black solid squares] only experiences 44% of the shielding, which is natural because the main shielding of H2 according to the found stacking pattern comes from the base to the 5′ end. In this case, that is the terminal G[1], which is expected to show increased dynamics and thereby, in average, spend less time shielding the following base. Panel B shows a projection of purine−purine stacking along the *Z*-axis taken from the crystal structure of the Dickerson−Drew dodecamer (DD). H8 protons are extruded into the major groove (green) while the H2 protons (red) are stacked under the shielding cone of the 3′ residue.

this pattern since the sequential distances between H6/H8$_n$ and (H1′, H2′″, H3′)$_{n-1}$ are all between 6.9 and 8.0 Å (Table 3). The presence of this NOE connectivity [H6/H8$_n$ to (H1′, H2′″, H3′)$_{n-1}$] for both the ssRNA and ssDNA hexamers (Figure 3, as well as Figure S4 in the Supporting Information) shows that the single-strand oligos do indeed spend a significant time in the NMR time scale occupying a right-handed helical conformation, which is typical of the A- or B-type double-stranded structures (*1a*). Significant contribution from a Z-type structure is ruled out because one would expect increased intensities of H6/H8$_n$−H5″″$_{n-1}$ cross-peaks compared to pure A- or B-type structures in the NOESY spectra since these distances are only 3.3 and 4.7 Å for Z-type conformation, to be compared with 6.9 and 7.2 Å for A-type and 6.2 and 6.7 Å for B-type conformation. All nucleobases are also in the anti conformation since in the syn conformation the H2 is further away from H1′ but H8 is closer to H1′ of the same residue, thus resulting in an increased intensity of the H8−H1′ cross-peak (Watson−Crick base pair, 3.5−3.8 Å; Hoogsteen base pair, ∼2.7 Å [*21*]) and the disappearance of the H2−H1′ cross-peak (Watson−Crick base pair, 4.2−4.5 Å; Hoogsteen base pair, ∼5.9 Å [*21*]). Since neither of these observations are made for either the ssRNA or ssDNA hexamers (**1a** and **1b**) (Figure 3), we conclude that the conformations statistically available to the single-strand hexamers at room temperature and below are dominated by right-handed conformations, even though it is void of stabilization from any hydrogen bond base pair formation.

D. Comparison of NOESY Footprints between ssDNA and ssRNA. A further comparison has been made between the NOESY footprints of the hexameric ssDNA (**1a**) and ssRNA (**1b**). The intraresidue H6/H8−H3′ (A-form, 3.2 Å; B-form, 4.4 Å) and H5−H3′ (A-form, 4.9 Å; B-form, 6.4 Å) cross-peaks, as well as the interresidue H6/H8−H3′$_{(n-1)}$ (A-form, 3.2 Å; B-form, 5.1 Å) and H5−H3′$_{(n-1)}$ (A-form, 4.9 Å; B-form, 6.4 Å) cross-peaks, are significantly stronger in the ssRNA hexamer than in the ssDNA counterpart (Figure 3A). In contrast, the interresidue H6/H8−H1′$_{(n-1)}$ (A-form, 4.3 Å; B-form, 3.0 Å) and H5−HH1′$_{(n-1)}$ (A-form, 5.0 Å; B-form, 3.8 Å) cross-peaks are stronger in ssDNA compared to ssRNA. Thus, the main differences between the ribo and the deoxy hexamers are found for the distances involving the H3′ proton (Figure 3E and Table S1 in the Supporting Information). This is expected since its relative position changes dramatically between the North and South sugar pucker modes (*1a*).

As reported above, the sugar proton $\sum^3 J_{H1'}$ couplings show that the central residues of the hexameric ssDNA are predominantly in South conformation, which is characteristic for B-type DNA duplex conformation, while the central residues of the hexameric ssRNA are predominantly in North conformation (Table 1), which is in turn associated with A-type conformation (*1a*). This suggests a predominant population of the A- and B-type helical conformation for ssRNA (1**b**) and ssDNA (1**a**), respectively, in the NMR time scale.

The differences between the two NOE footprints (Table 3 and Figure 3), associated with their preferred sugar conformations, strongly suggests that the ssDNA(**1a**) is not completely random coiled but rather has a substantial population of the preorganized B-type conformation while the ssRNA (**1b**) is preorganized to a large extent in an A-type conformation. To our knowledge, this is the first report of the NMR conformational features of native, unbound, stretched-out single-strand DNA and RNA that shows that the single-strand DNA or RNA is not completely in a random-coil state but they are preorganized into a right-handed helical conformation.

E. NMR-Constrained Molecular Dynamics (NMR-MD) Simulations of ssDNA and ssRNA. Based on the NMR observations above (see Experimental Procedures section for details), we have performed 1.5 ns of NMR-MD simulations (at 298 K) for both hexameric ssDNA and ssRNA (see Experimental Procedures section for details of NMR constraints, as well as for MD simulation protocol) using following NMR constraints: (a) 16 NMR constraints of the backbone dihedral angles (see Tables S2A and S2B for a list of dihedral constraints in the Supporting Information); (b) classification of observed NOE (diffusion) cross-peaks at τ_m = 800 ms into strong (1.8−5.0 Å) and weak (3.0−6.5

Table 2: Chemical Shifts of the H2 Protons in 2′-Deoxyadenosine 3′,5′-Bisphosphate **(3a)**, Hexameric ssDNA **(1a),** and the Adeninyl Residues of the Dodecamer (DD) at 273 and 363 K Presented To Compare Their Relative Diamagnetic Shielding Owing to the Intrastrand Stacking by the Neighboring Nucleobases[a]

compounds	proton	δ_{273K} (ppm)	$\Delta\delta_{27}$ (ppm)[b]	% shielding[d] (273 K)	δ_{363} (ppm)	$\Delta\delta_{363-273K}$ (ppm)[c]	% shielding[d] (363 − 273 K)
d(Etp**A**pEt)$_1$ (**3a**)	H2A	8.28			8.30		
d(G**A**^{1}**A**^{2}**A**^{3}**A**^{4}C)$_1$	H2A^1	7.65	0.63	58	7.99	0.34	44
	H2A^2	7.47	0.81	74	7.86	0.39	51
	H2A^3	7.41	0.87	80	7.86	0.45	58
	H2A^4	7.69	0.59	91	7.98	0.29	83
d(CGCG**A**^{5}**A**^{6}TTCGCG)$_2$	H2A^5	7.19	1.09	100	7.96	0.77	100
	H2A^6	7.63	0.65	100	7.98	0.35	100

[a] The δH2's of A^1, A^2, and A^3 residues in the d(GA^{1}A^{2}A^{3}A^{4}C)$_1$ (**1a**) are compared with the δH2 of the A^5 moiety in the DD [i.e., 5′-purine-adeninyl-purine-3′ sequence], while the δH2 of the A^4 residue in the d(GA^{1}A^{2}A^{3}A^{4}C)$_1$ (**1a**) is compared with that of the A^6 moiety in DD [i.e., 5′-purine-adeninyl-pyrimidine-3′ sequence]. [b] $\Delta\delta_{273K} = \delta_{H2A^n} - \delta_{H2\ EtpApEt}$ [i.e., difference between molecule (**1a**)/(DD) and (**3a**), Figure 1]. [c] $\Delta\delta_{363K-273K} = \delta_{H2A^n}$(363 K) $- \delta_{H2A^n}$(273 K) [molecule (**1a**)/(DD)]. [d] %shielding $= 100(\delta_{H2\ hexamer}/\delta_{H2\ duplex})$.

Å) cross-peaks leading to a total of 46 interresidue and 95 intraresidue distance constraints for ssDNA and of 41 interresidue and 70 intraresidue distance constraints for ssRNA. All interresidue NOE cross-peaks are summarized in Figure S3 in the Supporting Information. For the last 100 ps of the 1.5 ns long MD trajectory (Figure 4), we have collected snapshots every 10 ps that had an RMSD less than 1.0 Å (Table 4). These 10 structures are superimposed and shown in Figure 6 (panels A and B).

The MD simulation was also continued for another 1.5 ns without the NMR constraints at 298 K. The structures in this NMR-unconstrained MD (Figure 9) for both ssDNA and ssRNA were found to be distorted considerably giving an RMSD change of 6−8 Å for both single-stranded structures compared to the NMR-constrained structures shown in Figure 4. The comparison of the MD profiles in Figures 4 and 9 clearly shows the importance of the NMR constraints in the characteristic stacking geometries intrinsic in these structures, which also interestingly show that the single-stranded structures of DNA and RNA are not so random, they are indeed preorganized (Figure 6).

Simulations were also performed to make sure that enough conformational space was sampled in the MD simulations. An NMR constrained temperature cycling protocol (100 to 450 K and back to 100 K) of total 900 ps was also applied to the ssRNA and ssDNA for simulated annealing-like (SA) MD simulations, using the less preferred canonical form as starting structure (i.e., B-type conformation for ssRNA and A-type conformation for the ssDNA) in a solvated in a box filled with water molecules with added sodium ions. In these SA-MD runs, all NMR constraints used are the same as in the above MD protocol (Table S1 and Figure S3 in the Supporting Information). In these simulated annealing MD studies, the same final set of conformations were produced as those by the constrained MD protocol. The RMSD of the structures generated by SA protocol and those by the constrained MD protocol (Figure 4) is <1.8 Å for ssDNA and <1.7 Å for ssRNA.

F. Structural Analysis. The main difference between the calculated ssDNA and ssRNA structures lies in that they both retain the sugar phase angle, as well as the related χ torsion, that is preferred in duplex form also in single-strand form. Most interestingly, even though these results are expected from the $\sum^3 J_{H1'}$, the sugar and χ torsions also steer the stacking pattern differently in ssDNA and ssRNA. This manifests itself in offsets in roll, slide, and inclination that

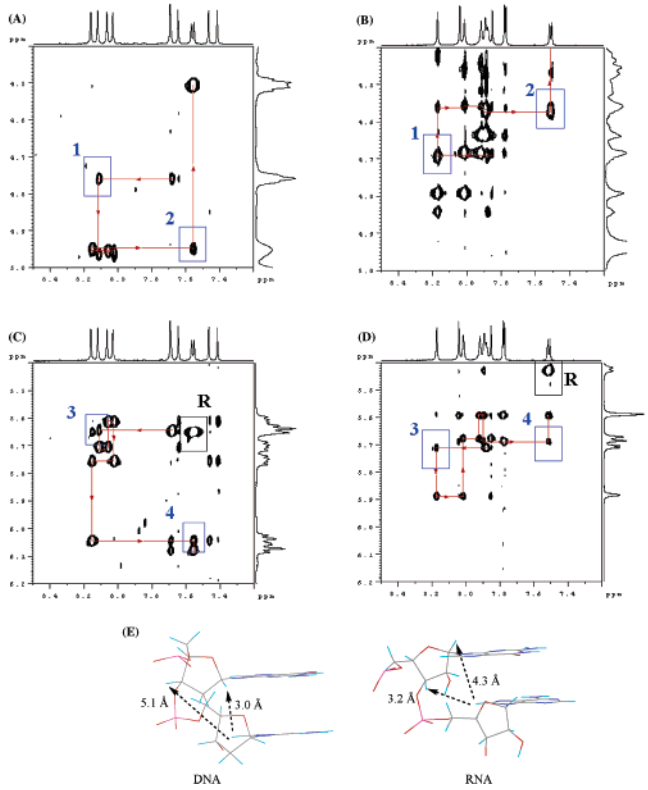

FIGURE 3: Pairwise comparison of the aromatic/H3′ region (A and B) and the aromatic/H1′ region (C and D) of NOESY spectra showing the main observed differences between ssDNA (**1a**) [A and C] and ssRNA (**1b**) [B and D]. The sequential H6/H8$_n$−H3′$_{(n-1)}$ cross-peaks (boxes 1 [H8A^1−H3′G] and 2 [H6C−H3′A^4], shown in panels A and B) are significantly stronger in the ssRNA (B) than in the ssDNA (A). The H6/H8$_n$−H3′$_{(n-1)}$ cross-peak in C3′-*endo* sugar conformation in ssRNA is stronger than that in ssDNA because the aromatic H8 and the H3′ in the former are in closer proximity due to their pseudoaxial orientation. In contrast, the aromatic H8 and the H3′ in ssDNA are both pseudoequatorial because of the sugar taking up the C2′-*endo* conformation. The H6/H8$_n$−H1′$_{(n-1)}$ cross-peaks (boxes 3 [H8A^1−H1′G] and 4 [H6C−H1′A^4], panels C and D), are found to be stronger for ssDNA (C) than for ssRNA (D) for the reversed structural argument (see panel E). The H5C−H6C cross-peak is used as the internal reference and is marked with box R in panels C and D. Panel E shows the structures of the G−A base step in a canonical B-DNA compared to that of the canonical A-RNA. They clearly show the characteristic shorter H6/H8$_n$−H1′$_{(n-1)}$ distance (3.0 Å) and longer H6/H8$_n$−H3′$_{(n-1)}$ distance (5.1 Å) in the DNA step, while the RNA step shows the opposite characteristics, longer H6/H8$_n$−H1′$_{(n-1)}$ and shorter H6/H8$_n$−H3′$_{(n-1)}$. This is reflected in their respective NOESY cross-peak intensities shown in Figure 4A.

Table 3: Experimental NOESY Crosspeak Data Compared with the Corresponding Expected Distances (Å) Measured in Models of the Single Strand of the Canonical A-, B-, and Z- Forms of DNA and RNA Duplexes[a]

	measured distances in canonical DNA/RNA			observed NOE cross-peaks	
distance	dsB-type	dsA-type	dsZ-type	ssDNA	ssRNA
H6/H8−H3′	4.37	**3.24**	5.13	M	**S**
H2−H2′″	7.02/5.84	4.63/5.38	5.83/4.63	−/W	M/#
H5−H3′	6.38	4.87	7.00	W	M
H6/H8−H1′$_{(n-1)}$	**3.01**	**4.34**	6.98	**S**	**S**
H6/H8−H3′$_{(n-1)}$	5.10	**3.25**	6.89	M	**S**
H5−H1′$_{(n-1)}$	3.80	5.00	5.18	M	W
H5−H3′$_{(n-1)}$	5.47	3.70	4.41	W	M
H2−H1′$_{(n-1)}$	4.64	**3.48**	5.20	M	S
H2− H′″$_{(n+1)}$	6.83/6.22	5.32/6.19	10.37/11.74	−/−	W/#
H2−H4′$_{(n+1)}$	5.69	6.32	6.81	W	−

[a] The observed cross-peaks have been categorized as strong, medium, or weak cross-peaks. Strong peaks are indicated in bold. [b] − indicates not detectable, W indicates weak (4−5.0 Å), M indicates medium (2.5−4 Å), S indicates strong (<3 Å), and # indicates that RNA is devoid of H2″.

are reminiscent of the double-stranded forms of B-DNA compared with A-RNA (Figure 5). If one considers the central adenine conformations, the significant structural parameters can be summarized as follows: ssRNA has sugar phase angles of 0−18°, χ torsions of 190−200°, roll of 0−10°, slide of −1 to −2 Å, and inclination of 0−15°. ssDNA has sugar phase angles of 145−165°, χ torsions of 260−300°, roll of −10° to −15°, slide of 2−3 Å, and inclination of −10° to −20°. Additional structural factors are available in the Supporting Information.

The NMR-MD derived geometry of the nucleobase overlap suggests that we have nearest-neighbor dispersion interactions with an attractive electrostatic character between the relatively electron-deficient pyrimidine and the relatively electron-rich imidazole moieties at each dinucleotide step. The important difference lies in the relative directionality of this interaction. The zooms highlighting the stacking geometries of each dinucleotide step of the hexameric ssDNA (**1a**) and ssRNA (**1b**) (Figure 6, panels C and D) show that the imidazole stacks above the pyrimidine in the 5′ to 3′ direction in ssDNA (**1a**) while, in contradistinction, the pyrimidine stacks above the imidazole in the 5′ to 3′ direction in ssRNA (**1b**). In ssDNA, the H2 protons are completely overlapped by the shielding cone of the base from the 5′-side ($n - 1$), while the H2 protons of ssRNA are mainly extruded and only partly shielded by the base from the 3′-side ($n + 1$). The situation is reversed for the H8 protons. In ssDNA, the H8 protons are extruded, while they receive full shielding by the base to the 5′-side ($n - 1$) in ssRNA. This means that the negative π-surface of one pyrimidine ring gets into the proximity of the relatively positive imino and amino hydrogens normally involved in base pairing of the $n + 1$ and $n - 1$ neighboring base for DNA and RNA, respectively.

The stability of two 9-adeninyl and two naphthyl groups joined by a three-atom linker (2-methylpropanoic acid) has been previously studied (*23*). Although theoretical calculations indicate that bis-naphthyl stacks better than bis-9-adeninyl groups in water (*22*), NMR experiments show the opposite (*23*). Luo et al. (*24*) explain this deviation from the expected result by the points of attachment of the linker to the aromatic rings being different in the two molecules, thereby more restricting the geometry available to stacked conformations for the bis-naphthyl than for the bis-adeninyl. The same reasoning can be used to explain the different stacking patterns found for ssDNA and ssRNA. Since the molecular compositions of the bases are identical for ssDNA and ssRNA, the obvious difference lies in the sugar−phosphate backbone motif (the "linker" for aglycones in nucleic acids), in that the sugar moiety of the former consists of 2′-deoxyribosyl moieties while the latter consists of ribosyl units. We draw the conclusion that, even though there are small differences in partial charges of the base atoms, the observed difference in stacking directionality in ssDNA and ssRNA originates from their respective preferred sugar conformations. Both the hexameric ssDNA and ssRNA maintain their respective sugar conformations that they prefer in duplex form (A-form for RNA and B-form for DNA), which has the effect that the orientation of the base relative to the sugar is different in ssDNA and ssRNA (pseudoequatorial in 2′-*endo*−3′-*exo* conformation versus pseudoaxial in 2′-*exo*−3′-*endo* conformation), and therefore the energetically available hyperspace for stacking is expected to be significantly different. Thus, the bases will be most probable to populate the lowest energy stacked conformation within the conformational hyperspace dictated by the sugar conformation.

G. Evaluation of Stacking Patterns. The chemical shifts of the ssDNA and ssRNA base protons have been used to identify and confirm the stacking pattern found in the MD simulations (Figure 6). The displacement of the H6, H8, and H2 protons in the $X-Y$ plane, relative to the closest ring atom of the neighboring bases ($n + 1$ and $n - 1$) have been measured and compared with the chemical shift shifts ($\Delta\delta$) obtained both from oligomerization and destacking processes. The oligomerization shift is defined as the difference in chemical shift between each proton inside the single-stranded oligomer and the chemical shift of the corresponding proton in monomer form. Oligomerization shifts are calculated for the individual nucleotide residues in the oligos (O_{oligo}) with respect to the corresponding monomeric nucleotide [dGpEt (**2a**)/GpEt (**2b**) or EtpdApEt (**3a**)/EtpApEt (**3b**) or EtpdC (**4a**)/EtpC (**4b**), Figure 1] (i.e., oligomerization shift = $\Delta\delta_{(\text{NpEt/EtpNpEt/EtpN}-O_{\text{oligo}})}$, in ppm, at 298 K). The different magnitudes of the upfield shifts (anisotropic shielding) of the different protons show how that particular proton experiences the aromatic ring current of the nearest neighboring nucleobase(s) (*7f,j*). The destacking shift is defined as the difference in the chemical shift for each base proton at low temperature (298 K) and high temperature (363 K) where any specific stacking is assumed distorted (i.e., destacking shift = $\Delta\delta_{363\text{K}-298\text{K}}$, raw data in Figure S5 in the Supporting Information). The displacements (Å) of the marker protons relative to the neighboring bases, and thus the stacking shielding, are extracted from the average structures of the final 100 ps MD simulations of the single-stranded DNA and RNA (see the Experimental Procedures section for details of the MD simulations and the calculation of the shielding factors from the displacement).

Linear regression plots of the oligomerization or destacking shifts of the marker protons versus their respective shielding factors have been made (Figure 7A,B). The *Y*-axis (shielding) is calculated directly from the coordinates of the final MD

Table 4: RSMDs of ssDNA and ssRNA Structures[a]

		all atoms		backbone atoms		heavy atoms	
		G...C[c]	$A^1...A^4$ [c]	G...C[c]	$A^1...A^4$ [c]	G...C[c]	$A^1...A^4$ [c]
1	ssDNA	0.61 ± 0.14	0.41 ± 0.08	0.49 ± 0.13	0.29 ± 0.07	0.57 ± 0.14	0.38 ± 0.08
2	ssRNA	0.65 ± 0.09	0.48 ± 0.11	0.50 ± 0.11	0.33 ± 0.09	0.59 ± 0.08	0.45 ± 0.11
3	ssDNA	2.72 ± 0.20	2.23 ± 0.11	2.17 ± 0.19	1.55 ± 0.06	2.55 ± 0.19	2.09 ± 0.11
4	ssRNA	2.21 ± 0.21	1.64 ± 0.18	1.35 ± 0.26	0.65 ± 0.16	2.05 ± 0.22	1.45 ± 0.20

[a] Entries 1 and 2 show the RMSD between 10 snapshots from the last 100 ps of the total MD simulation (1.5 ns, see Experimental Procedures section) and their respective average structures during the last 100 ps for ssDNA (entry 1) and ssRNA (entry 2), thereby showing the rms deviation within the respective group of structures. Entries 3 and 4 show the RMSD between the same 10 snapshots during the last 100 ps and the corresponding canonical single strand for the ssDNA (B-DNA) and ssRNA (A-RNA). [b] Values include all six residues from G to C (note higher RMSD originates from relatively larger motion of the terminal residues). [c] Values include four middle residues from A^1 to A^4 in which motions are relatively more restricted.

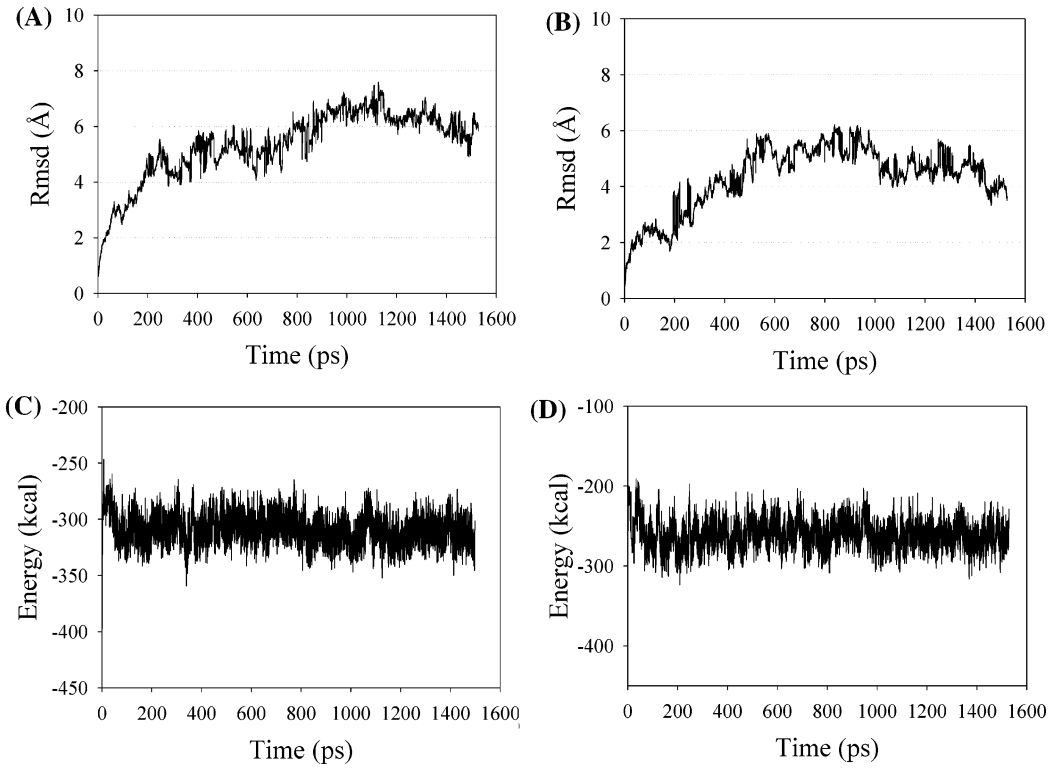

FIGURE 4: Panel A shows the mass-weighted RMSD between the ssDNA (**1a**) molecular modeling trajectory and the minimized starting structure. Panel B shows the mass-weighted RMSD between the ssRNA (**1b**) molecular modeling trajectory and the minimized starting structure. Panel C shows the total potential energy of the ssDNA (**1a**) with all constraints switched on. Panel D shows the total potential energy of the ssRNA (**1b**) with all constraints switched on.

structures, while the *X*-axis ($\Delta\delta$) is calculated from raw NMR data. A high degree of correlation is found for both the plot using the oligomerization shift ($R = 0.83$, Figure 7A) and the plot using the destacking shift ($R = 0.82$, Figures 7B) as $\Delta\delta$ source on the *X*-axis. It is noteworthy that the same kind of correlation plots, instead using strands in canonical A- and B-type conformation as structural input on the *Y*-axis, gives a lower linear correlation factor ($R = 0.69$ for oligomerization and $R = 0.68$ for destacking shift [plots not shown]), thus giving some indication of the sensitivity of this method.

These back calculations of the predicted shielding effects on the chemical shifts of the base protons validate the base−base stacking pattern of the ssDNA and ssRNA hexamers produced by the MD simulations. The clear difference between the deoxy and the ribo hexamers is highlighted by the complete absence of correlation when the coordinates are swapped between the two ($R = 0.077$ for oligomerization and $R = 0.070$ for destacking shift, plot not shown).

Even though both H2 and H8 protons from ssRNA, as well as ssDNA, fall on the same line when correlated with the proton coordinates, the H2 protons are much more sensitive markers than the H8 protons due to their accurate and systematically different distribution for ssRNA and ssDNA (Figure 7). This is a direct reflection of the fact that the microenvironments around the H2 protons are distinctly different in ssDNA and ssRNA.

The two methods used to estimate the degree of relative shielding of each base proton are fully correlated, $R = 0.92$ for the ssDNA protons and $R = 0.97$ for the ssRNA protons (Figure 8). There is however a 0.1 ppm offset, most likely originating from that the ssDNA protons receive more shielding from the rapid motions at high temperature (δ_{363K}). This would be the result of that ssDNA become less distorted by the increased dynamics and maintain stacking at higher temperatures than ssRNA, due to better flexibility or somewhat more stable stacking or both of ssDNA compared to ssRNA. As can be seen in Figure 7A,B, this does not

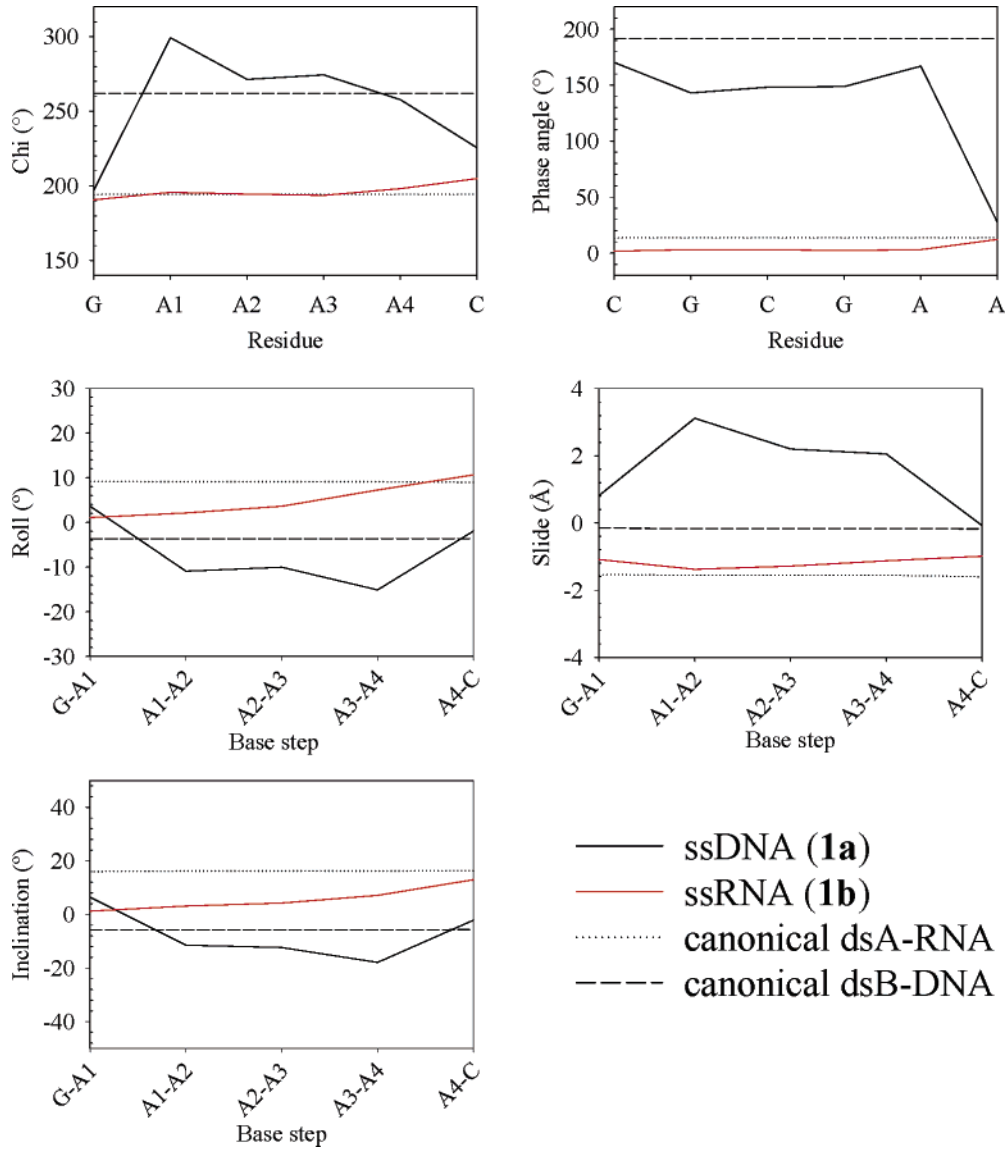

FIGURE 5: A summary of the backbone and helical parameters that differ significantly between ssDNA (**1a**, black) and ssRNA (**1b**, red). A complete compilation of the helicals and dihedrals are presented in Figure S4 in the Supporting Information.

further add to the error of the method, the main contribution to the error comes from the fact that the structural input for each base step in the correlation (*Y*-axis shielding value) originates from a conformation that is only populated to 50−80% and, therefore, includes a large unavoidable uncertainty factor when studying molecules with significant internal motion.

DISCUSSION

The different adeninyl−adeninyl stacking modes of ssDNA in relation to ssRNA manifest themselves in several phenomena that have been observed in this lab (*7*) and in other laboratories (*2*, *5*, *6*). pH titration studies (*7f,j*) have shown that the aromatic protons along the chain in ssRNA show a pK_a variation of ∼0.2 units of the guanine imino proton in the 5′-GAAAAC-3′ sequence. The isosequential ssDNA shows variations of ∼0.9 units, which directly reflects the efficiency of modulation by the different base−base stacking patterns, together with the micromagnetic field gradients from nearby electrons experienced by the different marker protons, as the respective stacks are perturbed by the deprotonation.

The same works (*7f,j*) have also shown that the pK_a of the guanine imino proton itself is modulated by the different stacking patterns in ssDNA and ssRNA. In ssRNA, the pyrimidine ring of the neighboring adeninyl shields the imino proton from the 3′ end but not from the 5′ end. The reverse is true for ssDNA where the pyrimidine ring of the neighboring adeninyl shields the imino proton from the 5′ end but not from the 3′ end. This positions the relatively electron-rich surface of the pyrimidine ring close to the relatively positive imino proton of the guaninyl. Directional differences in pK_a have been reported (*7f,j* and Table S3 in the Supporting Information): for ssRNA and ssDNA, 5′-r(GAAC)-3′ (9.76) and 5′-r(CAAG)-3′ (9.43), 5′-rCGA-3′ (10.25) and 5′-rAGC-3′ (10.05), while the trend is opposite in 5′-dCGA-3′ (10.01) and 5′-dAGC-3′ (10.10). Thus, the guanine is less prone to release its imino proton when it stacks to the 5′-end of a purine in ssRNA and to the 3′-end of a purine in ssDNA. This may be due to direct electrostatic charge modulation between the stacking bases or through

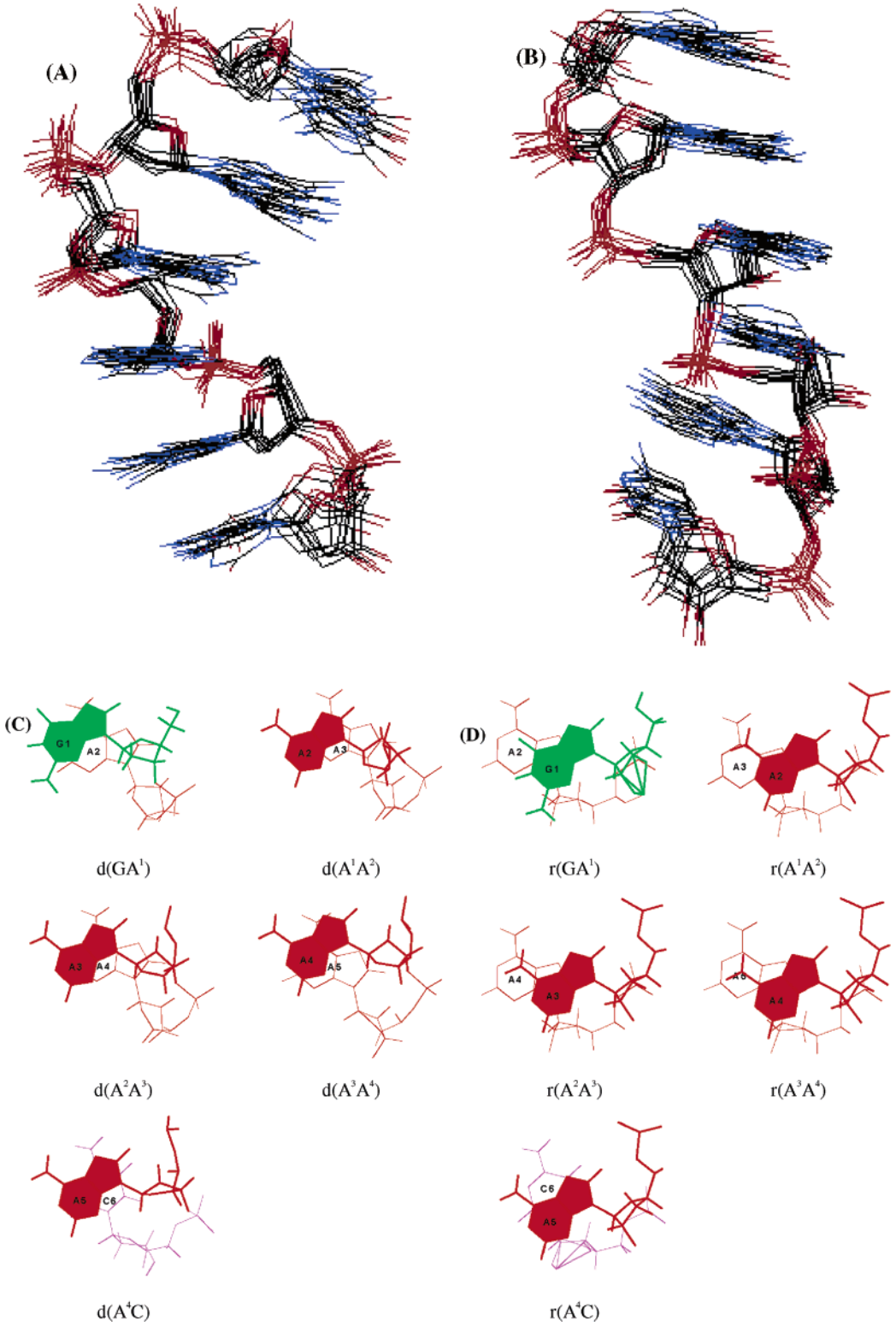

FIGURE 6: Superimpositions of the MD snapshots and zooms highlighting the stacking geometries of each dinucleotide step of the hexameric ssDNA (**1a**) and ssRNA (**1b**). Panels A and B show the superimpositions of 10 snapshots from the last 100 ps of the 1.5 ns MD run for ssDNA (**1a**) and ssRNA (**1b**), respectively. Panels C and D show the stacking geometry at each dinucleotide step of the minimized average structure of the last 100 ps of the 1.5 ns MD simulation for ssDNA (**1a**) and ssRNA (**1b**), respectively. Note that the imidazole stacks above the pyrimidine (5′→3′) in ssDNA (**1a**) while, on the contrary, the pyrimidine stacks above the imidazole (5′→3′) in ssRNA (**1b**).

interactions between the neighboring base and the solvent, making it harder for the negative OH^- both to approach and to withdraw the imino proton. A more general observation (*7j*) is that a guanine flanked by two pyrimidines always has a lower pK_a than a guanine flanked by two purines (Table S3 in the Supporting Information), thus underlining the general importance of nearest-neighbor screening for imino proton reactivity. [Although the stacking geometry is only one variable affecting the pK_a of a proton, it is possible to correlate the pK_a of different single-strand oligomers to the $X-Y$ displacement of the imino proton relative to the positions of the neighboring bases using the stacking

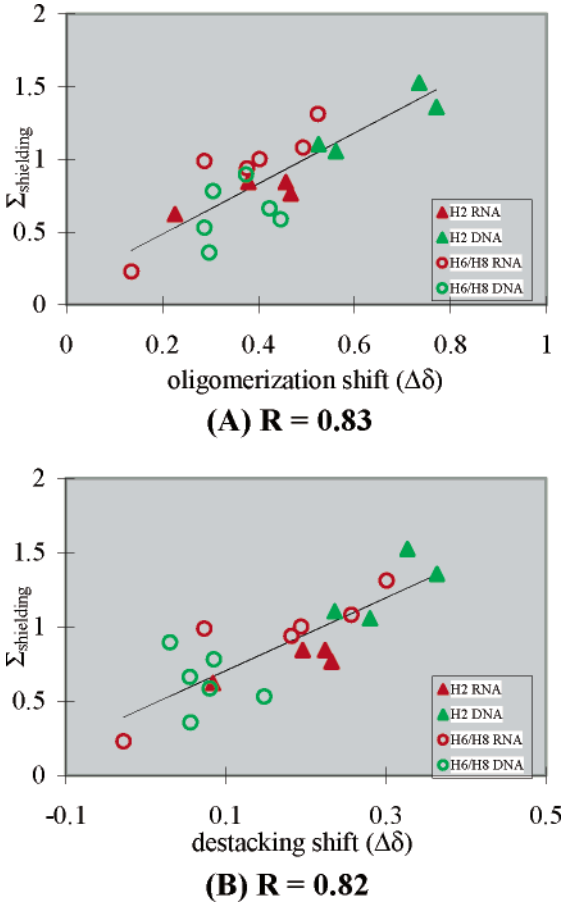

FIGURE 7: Correlation plots between the oligomerization shift (A, $R = 0.83$) and destacking shift (B, $R = 0.82$) versus the combined effect (the displacement in the $X-Y$ plane of each proton (H8, H2, and H6) from the nearest edge of the neighboring nucleobase was measured in both 3′ and 5′ directions; the distances were then normalized to a sigmoidal, $y = 1 - 1/\{1 + 10^{[(2-x)/2]}\}$, and summed to give a value proportional to the shielding received from the neighboring ring systems (see Experimental Procedures section)) of the neighboring bases for the modeled ssDNA **(1a)** and ssRNA **(1b)**. The relatively good correlation validates the observed stacking patterns in the ssDNA and ssRNA simulations. There are no correlations of the modeled ssDNA **(1a)** and ssRNA **(1b)** when the oligomerization shifts ($R = 0.077$) and destacking shifts ($R = 0.070$) have been swapped between the RNA and DNA structures, thus showing that there is really a significant difference between the stacking patterns of the two hexamers.

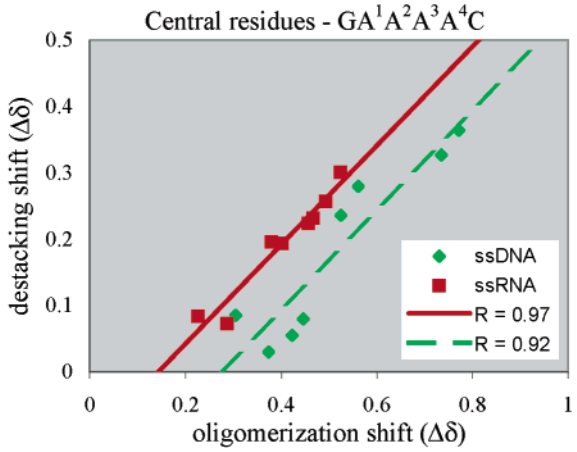

FIGURE 8: Correlation plot of the adeninyl protons between the oligomerization shifts and the destacking shifts. The two methods used to estimate the amount of shielding at each base proton are fully correlated, $R = 0.92$ for ssDNA and $R = 0.97$ for ssRNA. There is however a 0.1 ppm offset, most likely originating from the ssDNA protons receiving more shielding from the rapid motions at high temperature (δ_{363K}). The same correlation using the points of both ssDNA and ssRNA together have a correlation factor of $R = 0.86$.

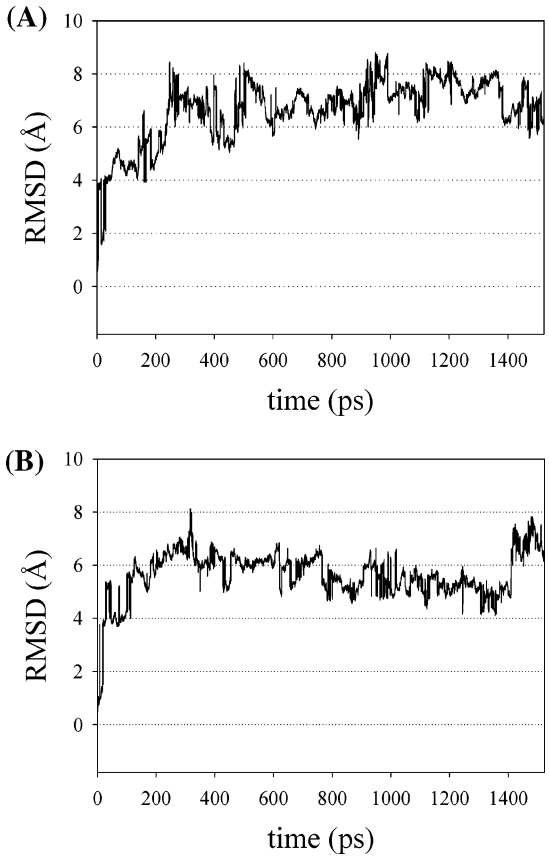

FIGURE 9: The mass-weighted RMSDs of the MD trajectories (1.5 ns) obtained upon gradual release of the NMR constraints from the final structures of the NMR-constrained MD trajectories in Figure 4 for ssDNA (**1a**, A) and ssRNA (**1b**, B). The final NMR constrained structures in Figure 4A,B are used as the starting point as well as for reference for the NMR-unconstrained MD to show the distortion of the structures from the point where the NMR constraints are released. This gives a distortion of 6−8 Å for both single-stranded structures after 1.5 ns of free MD at 298 K.

model from the MD studies in this work. Fourteen ssDNA sequences and 11 ssRNA sequences give a correlation factor of 0.66 (Figure S6 in the Supporting Information).]

Another interesting phenomenon that can be correlated to the different stacking in ssDNA and ssRNA is the duplex stabilization by dangling-end residues. This directional specificity of dangling-end stabilization (*6*) can be directly correlated to the amount of screening the dangling-end motif provides for the hydrogen bonds of the closing base pair and is fully consistent with the stacking model suggested in this paper. A 5′-dangling end residue following the ssDNA stacking geometry will position itself over and protect the closing base pair while the corresponding ssRNA stacking will position the dangling base away from the closing base pair and vice versa for 3′-dangling ends. Thus, the observed stacking patterns provide a rationale for the direction-specific stabilization provided by dangling base overhangs in DNA and RNA (*6*).

CONCLUSIONS

(1) The endocyclic $^3J_{HH}$ of the sugar moieties of the single-stranded ssRNA and ssDNA show that the constituent sugars maintain their preferred average conformations even though there is no hydrogen bond stabilization through base pair formation (Table 1). The central adenine bases spend 50−80% of the time in stacked conformation as evident from the comparison of chemical shifts (Table 2).

(2) The NOESY footprints of the ssRNA and ssDNA oligomers show *both* intra- and interresidue cross-peaks the relative intensities of which place ssRNA in an NMR time average conformation that is more of A-type than either B- or Z-type and vice versa for ssDNA, which is more of B-type.

(3) The NMR-MD derived geometries of the nucleobase overlaps at each dinucleotide step of the hexameric ssDNA (**1a**) and ssRNA (**1b**) show that the electron-rich imidazole stacks above the electron-deficient pyrimidine in the 5′ to 3′ direction in ssDNA (**1a**) while the pyrimidine stacks above the imidazole (5′ to 3′) in ssRNA (**1b**) (Figure 6) in purine−purine stacking. This places the negative π-surface of one pyrimidine ring into the proximity of the more positive imino and amino hydrogens normally involved in base pairing of the $n + 1$ and $n - 1$ neighboring bases for DNA and RNA, respectively.

(4) The shielding experienced by each base proton in the oligomer compared to its chemical shift in monomer form and the high temperature destacked state is systematically different in ssDNA and ssRNA (Figure 8). The $X-Y$ displacement of each proton relative to the shielding cones of the neighboring ring systems correlate with the difference in chemical shift of that particular proton due to oligomerization ($R = 0.83$) and destacking ($R = 0.82$). The coordinates of the corresponding oligomer MD simulation are used to estimate the influence of the neighboring bases (see Experimental Procedures section). This correlation is completely lost ($R = 0.07$) when the coordinates for ssDNA and ssRNA are reversed.

(5) In ssRNA, the δH8A is relatively more deshielded by pH titration ($\Delta\delta = \delta_{pH12} - \delta_{pH7}$) compared to that of δH2A. This trend is reversed in ssDNA in which δH2A changes more compared to that of δH8A (*7f,j*). This shows that the marker protons experience different shielding gradients upon pH-induced perturbation in ssDNA and ssRNA, thus strongly indicating that the orientation of the base−base stacking in the ground state is different in the two, and hence they have different spatial positions relative to the shielding cones of the neighboring bases.

(6) Directional differences in the base−base stacking interactions and the resulting conformational changes (Table S3 in the Supporting Information [*7f,j*]) could alter the hydration properties around the aglycones in a variable manner, which could play a key role in the perturbation of the pK_a observed for the 9-guaninyl in different isosequential ssDNAs and ssRNAs.

(7) That the NMR constraints indeed reflect the present structures of the ssDNA and ssRNA has been demonstrated unambiguously by the fact that mass-weighted RMSDs of the structures (harvested through the MD trajectories for 1.5 ns) obtained upon gradual release of the NMR constraints from the final NMR-constrained structures show a distortion of 6−8 Å for both single-stranded structures after 1.5 ns of free MD at 298 K.

SUPPORTING INFORMATION AVAILABLE

Table S1 providing a summary of all interproton distances (from NOESY) used for structure evaluation of DNA and RNA; Table S2 giving the dihedral and sugar phase angle and puckering amplitude constraints (from NMR) used in the molecular modeling simulations; Table S3 giving a comparison of sequence-dependent pK_a and $\Delta G^{ob}_{pK_a}$ of the 9-guanylate ions; Table S4 displaying ^{1}H chemical shifts [δ_H, ppm] at neutral (N) and deprotonated (D) states at 298 K for monomeric (**2a**, **2b**, **3a**, **3b**, **4a**, **4b**) and hexameric (**1a**, **1b**) ssDNA and ssRNA; Figure S1 showing NMR assignments for compounds **1a** and **1b**; Figure S2 showing oligomerization shifts at 298 K for the aromatic protons in ssDNAs (**1a)** and ssRNAs (**1b)**; Figure S3 showing the interresidue cross-peaks used in the structure generation for ssDNA (**1a**) and ssRNA (**1b**); Figure S4 providing a comparison of the backbone dihedrals and helical paramters of the average structures of the final 100 ps of the MD simulation between ssDNA (**1a**) and the ssRNA (**1b**); Figure S5 showing the temperature-dependent drift of the ssDNA and ssRNA aromatic protons due to kinetically driven destacking; Figure S6 giving the shielding coefficient of the imino proton of G calculated using the stacking pattern for dGAAAAC and rGAAAAC plotted versus the pK_a. This material is available free of charge via the Internet at http://pubs.acs.org.

REFERENCES

1. (a) Saenger, W. (1988) *Principles of Nucleic Acid Structure*, Springer-Verlag, Berlin. (b) Bloomfield, V. A., Crothers, D. M., and Tinoco, I. (1999) *Nucleic Acids: Structures, Properties and Functions*, University Science Books, Sausalito, CA. (c) Leninger, A. L., Nelson, D. L., and Cox, M. M. (1993) *Principles of Biochemistry*, 2nd ed., Worth Publishers Inc., New York. (d) Sponer, J., Leszczynski, J., and Hobza, P. (1996) Nature of nucleic acid−base stacking: nonemperical ab initio and empirical potential characterization of 10 stacked base dimmers. Comparison of stacked and H-bonded base pairs, *J. Phys. Chem. 100*, 5590−5596. (e) Renugopalakrishnan, V., Lakshminarayanan, A. V., and Sasishekharan, V. (1971) Stereochemistry of nucleic acids and polynucleotides. III. Electronic charge distribution, *Biopolymers 10*, 1159−1167. (f) Joule, J. A., and Mills, K. (2000) *Heterocyclic Chemistry*, 4th ed., Blackwell Science, Oxford, U.K. (g) Schindler, M. (1988) Magnetic Properties in Terms of Localized Quantities. 9. The DNA Bases and the Protonation of Adenine, *J. Am. Chem. Soc. 110*, 6623−6630 and references therein. (h) Cantor, C. R., and Schimmel, P. R. (1980) *Biophysical Chemistry: The Conformation of Biological Macromolecules*, W H Freeman & Co., San Francisco, CA.
2. (a) Kool, E. T. (2001) Hydrogen Bonding, Base Stacking, and Sterric Effects in DNA Replication, *Annu. Rev. Biophys. Biomol. Struct. 30*, 1−22 and references therein. (b) Braasch, D. A., Jensen, S., Liu, Y., Kaur, K., Arar, K., White M. A., and Corey, D. R. (2003) RNA Interference in Mammalian Cells by Chemically-Modified RNA, *Biochemistry 42*, 7967−7975. (c) Grünweller, A., Wyszko, E., Bieber, B., Jahnel, R., Erdmann, V. A., and Kurreck, J. (2003) Comparison of different antisense strategies in mammalian cells using locked nucleic acids, 2′*O*-methyl RNA, phosphorothioates and small interfering RNA, *Nucleic Acids Res. 31*, 3185−3193. (d) Rosel Kretschmer-Kazemi, R., and Sczakiel, G. (2003) The activity of siRNA in mammalian cells is related to structural target accessibility: a comparison with antisense oligonucleotides, *Nucleic Acids Res. 31*, 4417−4424. (e) Cerritelli, S. M., and Crouch, R. J. (1988) Cloning, Expression, and Mapping of Ribonucleases H of Human and Mouse Related to Bacterial RNase H1, *Genomics 53*, 300−307. (f) Nielson, P. E. (1999)

Peptide Nucleic Acid. A Molecule with Two Identities, *Acc. Chem. Res. 32*, 624−630. (g) Barawkar, D. A., and Bruice, T. C. (1999) Deoxynucleic Guanidines/PNA (DNG/PNA) Chimeras: Oligonucleotide Analogue Containing Cationic Guanidium and Neutral Amide Linkage, *J. Am. Chem. Soc. 121*, 10418−10419. (h) Wengel, J. (1999) Synthesis of 3′-C- and 4′-C-Branched Oligodeoxynucleotides and the Development of Locked Nucleic Acid (LNA), *Acc. Chem. Res. 32*, 301−310. (i) Herdewijn, P. (1999) Conformationally restricted carbohydrate-modified nucleic acids and antisense technology, *Biochim. Biophys. Acta 1489*, 167−179. (j) Chaput, J. C., Ichida, J. K., and Szostak, J. W. (2003) DNA Polymerase-Mediated DNA Synthesis on a TNA Template, *J. Am. Chem. Soc. 125*, 856−857. (k) Zhu, L., Lukeman, P. S., Canary, J. W., and Seeman, N. C. (2003) Nylon/DNA: Single-Stranded DNA with a Covalently Stitched Nylon Lining, *J. Am. Chem. Soc. 125*, 10178−10179. (l) Seeman, N. C. (1999) DNA engineering and its application to nanotechnology, *Trends Biotechnol. 17*, 437−443. (m) Li, X, and Liu, D. R. (2003) Stereoselectivity in DNA-Templated Organic Synthesis and its Origins, *J. Am. Chem. Soc. 125*, 10188−10189.

3. (a) Chan, S. I., and Nelson, J. H. (1969) Proton Magnetic Resonance Studies of Ribose Dinucleoside Monophosphates in Aqueous Solution. I. The Nature of the Base-Stacking Interaction in Adenylyl (3′-5′)adenosine, *J. Am. Chem. Soc. 91*, 168−183. (b) Altona, C. (1975) in *Structure and Conformation of Nucleic Acids and Protein- Nucleic Acid Interactions*, (Sundaralingam, M., and Rao, S. T., Eds.) p 613, University Park Press, Baltimore, MD. (c) Lee, C.-H., Ezra, F. S., Kondo, N. S., Sarma, R. H., and Danyluk, S. (1976) Conformational Properties of Dinucleoside Monophosphates in Solution: Dipurines and Dipyrimidines, *Biochemistry 15*, 3627−3639. (d) Olsthoorn, C. S. M., Bostelaar, L. J., de Rooij, J. F. M., and van Boom, J. H. (1981) Circular dichroism study of stacking properties of oligodeoxyadenylates and polydeoxyadenylate. A three-state conformational model, *Eur. J. Biochem. 115*, 309−321. (e) Simpkins, H., and Richards, E. G. (1967) Titration Properties of Some Dinucleotides, *Biochemistry 6*, 2513−2520. (f) Luo, R., Gilson, H. S. R., Potter, J., and Gilson, M. K. (2001) The Physical Basis of Nucleic Acid Base Stacking in Water, *Biophys. J. 80*, 140−148. (g) Broom, A. D., Schweizer, M. P., and Ts'O, P. O. P. (2003) DNA Polymerase-Mediated DNA Synthesis on a TNA Template, *J. Am. Chem. Soc. 125*, 856−857. (h) Warshaw, M. M., and Tinoco, I., Jr. (1965) Absorption and optical rotatory dispersion of six dinucleoside phosphates, *J. Mol. Biol. 13*, 54−64. (i) Davis, R. C., and Tinoco, I., Jr. (1968) Temperature-dependent properties of dinucleoside phosphates, *Biopolymers, 6*, 223−242. (j) Lee, C. H., and Tinoco, I., Jr. (1980) Conformation Studies of 13 Trinucleoside Diphosphates by 360 MHz PMR Spectroscopy. A Bulged Base Conformation. I. Base Protons and H1′ Protons, *Biophys. Chem. 11*, 283−294. (k) Powell, J. T., Richards, E. G., and Gratzer, W. B. (1972) The nature of stacking equilibria in polynucleotides, *Biopolymers 11*, 235−250.

4. (a) Anderson, E. M., Halsey, W. A., and Wuttke, D. S. (2003) Site-Directed Mutagenesis Reveals the Thermodynamic Requirements for Single-Stranded DNA Recognition by the Telomere-Binding Protein Cdc 13, *Biochemistry 42*, 3751−3758. (b) Nishinaka, T., Ito, Y., Yokoyama, S., and Shibata, T. (1997) An extended DNA structure through deoxyribose-base stacking induced by RecA protein, *Proc. Natl. Acad. Sci. U.S.A. 94*, 6623−6628. (c) Toulmé, J.-J. (1985) Stacking interactions: the key mechanism for binding of proteins to single-stranded regions of native and damaged nucleic acids? *NATO ASI Ser., Ser. A, Life Sci. 101*, 263. (d) Vesnaver, G., and Breslauer, K. J. (1991) The contribution of DNA single-stranded order to the thermodynamics of duplex formation, *Proc. Natl. Acad. Sci. U.S.A. 88*, 3569−3573. (e) Weinfeld, M., Soderlind, K.-J. M., and Buchko, G. W. (1993) Influence of nucleic acid base aromaticity on substrate reactivity with enzymes acting on single-stranded DNA, *Nucleic Acids Res. 21*, 621−62., (f) Bar-Ziv, R., and Libchaber, A. (2001) Effects of DNA sequence and structure on binding of RecA to single-stranded DNA, *Proc. Natl. Acad. Sci. U.S.A. 98*, 9068−9073. (g) Igoucheva, O., Alexeev, V., and Yoon, K. (2001) Targeted gene correction by small single-stranded oligonucleotides in mammalian cells, *Gene Ther. 8*, 391−399. (h) Wadsworth, R. I. M., and White, M. F. (2001) Identification and properties of the crenarchaeal single-stranded DNA binding protein from *Sulfolobus solfataricus*, *Nucleic Acids Res. 29*, 914−920. (i) Ren, J., and Chaires, J. B. (1999) Sequence and Structural Selectivity of Nucleic Acid Binding Ligands, *Biochemistry 38*, 16067−16075. (j) Zhu, J., and Wartell, R. M. (1997) The Relative Stabilities of Base Pair Stacking Interactions and Single Mismatches in Long RNA Measured by Temperature Gradient Gel Electrophoresis, *Biochemistry 36*, 15326−15335. (k) Bochkareva, E., Belegu, V., Korolev, S., and Bochkarev, A. (2001) Structure of the major single-stranded DNA-binding domain of replication protein A suggests a dynamic mechanism for DNA binding, *EMBO J. 20*, 612−618. (l) Aalberts, D. P., Parman, J. M., and Goddard, N. L. (2003) Single-Strand Stacking Free Energy from DNA Beacon Kinetics, *Biophys. J. 84*, 3212−3217. (m) Schueler, W., Dong, C.-Z., Wecker, K., and Roques, B. P. (1999) NMR Structure of the Complex between the Zinc Fingure Protein NCp10 of Moloney Murine Leukemia Virus and the Single-Stranded Pentanucleotide d(ACGCC): Comparison with HIV−NCp7 Complexes, *Biochemistry 38*, 12984−12994. (n) South, T. L., and Summers, M. F. (1993) Zinc- and sequence-dependent binding to nucleic acids by the N-terminal zinc finger of the HIV-1 nucleocapsid protein: NMR structure of the complex with the Psi-site analogue, dACGCC, *Protein Sci. 2*, 3−19. (o) Braddock, D. T., Baber, J. L., Levens, D., and Clore, G. M. (2002) Molecular basis of sequence-specific single-stranded DNA recognition by KH domains: solution structure of a complex between hnRNP K KH3 and single-stranded DNA, *EMBO J. 21*, 3476−3485. (p) Chou, S.-H., Chin, K.-H., and Chen, F.-M. (2002) Looped out and perpendicular: Deformation of Watson−Crick base pair associated with actinomycin D binding, *Proc. Natl. Acad. Sci. U.S.A. 99*, 6625−6630. (q) Kwon, Y., Xi, Z., Kappen, L. S., Goldberg, I. H., and Gao, X. (2003) New Complex of Post-Activated Neocarzinostatin Chromophore with DNA: Bulge DNA Binding from the Minor Groove, *Biochemistry 42*, 1186−1198. (r) Mao, B., Gu, Z., Gorin, A., Hingerty, B. E., Broyde, S., and Patel, D. J. (1997) Solution Structure of the Aminofluorene-Stacked Conformer of the syn [AF]-C^8-dG Adduct Positioned at a Template-Primer Junction, *Biochemistry 36*, 14491−14501. (s) Lingel, A., Simon, B., Izaurralde, E., and Sattler, M. (2004) Nucleic acid 3′-end recognition by the Argonaute2 PAZ domain, *Nat. Struct. Mol. Biol. 11*, 576−577.

5. (a) McFail-Isom, L., Shui, X., and Williams, L. D. (1998) Divalent Cations Stabilize Unstacked Conformations of DNA and RNA by Interacting with Base II System, *Biochemistry 37*, 17105−17111. (b) Rooman, M., Liévin, J., Buisine, E., and Wintjens R. (2002) Cation-π/H-bond Stair Motifs at Protein-DNA Interfaces, *J. Mol. Biol. 319*, 67−76. (c) Umezawa, Y., and Nishio, M. (2002) Thymine-methyl/π interaction implicated in the sequence-dependent deformability of DNA, *Nucleic Acids Res. 30*, 2183−2192. (d) Zacharias, N., and Dougherty, D (2002) Cation-π interactions in ligand recognition and catalysis, *Trends Pharmacol. Sci. 23*, 281−287 and references therein. (e) Boehr, D. D., Farley, A. R., Wright, G. D., and Cox, J. R. (2002) Analysis of the $\pi-\pi$ Stacking Interactions between the Aminoglycoside Antibiotic Kinase APH-(3′)-IIIa and its Nucleotide Ligands, *Chem. Biol. 9*, 1209−1217. (f) Tatko, C. D., and Waters, M. L. (2002) Selective Aromatic Interactions in β-Hairpin Peptides, *J. Am. Chem. Soc. 124*, 9372−9373. (g) Butterfield, S. M., Patel, P. R., and Water, M. L. (2002) Contribution of Aromatic Interaction to α-Helix Stability, *J. Am. Chem. Soc. 124*, 9751−9755. (h) Tsou, L. K., Tatko, C. D., and Waters, M. L. (2002) Simple Cation-π Interaction between a Phenyl Ring and a Protonated Amine Stabilizes an α-Helix in Water, *J. Am. Chem. Soc. 124*, 14917−14921. (i) Gervasio, F. L., Chelli, R., Procacci, P., and Schettino, V. (2002) The nature of intermolecular interactions between aromatic amino acid residues, *Proteins: Struct., Funct., Genet. 48*, 117−125. (j) Zhou, Z., and Swenson, R. P. (1996) The Cumulative Electrostatic Effect of Aromatic Stacking Interactions and the Negative Eletrostatic Environment of the Flavin Mononucleotide Binding Site Is a Major Determinant of the Reduction Potential for the Flavodoxin from *Desulfovibrio vulgaris* [Hildenborough], *Biochemistry 35*, 15980−15988. (k) Gallivan, J. P., and Dougherty, D. (1999) Cation-π interactions in structural biology, *Proc. Natl. Acad. Sci. U.S.A. 96*, 9459−9464. (l) Biot, C., Buisine, E., Kwasigroch, J.-M., Wintjens, R., and Rooman, M. (2002) Probing the Energetic and Structural Role of Amino Acid/Nucleobase Cation-π Interactions in Protein−Ligand Complexes, *J. Biol. Chem. 277*, 40816. (m) Wintjens, R., Liévin, J., Rooman, M., and Buisine, E. (2000) Contribution of Cation-π Interactions to the Stability of Protein-DNA Complexes, *J. Mol. Biol. 302*, 395−410. (n) Hu, G.,

Gershon, P. D., Hodel, A. E., and Quiocho, F. A. (1999) mRNA cap recognition: Dominant role of enhanced stacking interactions between methylated bases and protein aromatic side chain, *Proc. Natl. Acad. Sci. U.S.A. 96*, 40816−40822.

6. (a) Burkard, M. E., Kierzek, R., and Turner, D. H. (1999) Thermodynamics of Unpaired Terminal Nucleotides on Short RNA Helixes Correlates with Stacking at Helix Termini in Larger RNAs, *J. Mol. Biol. 290*, 967−982 and references therein. (b) Kim, J., Walter, A. E., and Turner, D. H. (1996) Thermodynamics of Coaxially Stacked Helixes with GA and CC Mismatches, *Biochemistry 35*, 13753−13761. (c) Bommarito, S., Peyret, N., and SantaLucia, J., Jr. (2000) Thermodynamic parameters for DNA sequences with dangling ends, *Nucleic Acids Res. 28*, 1929−1934. (d) Rosemeyer, H., and Seela, F. (2002) Modified purine nucleosides as dangling ends of DNA duplexes: the effect of the nucleobase polarizability on stacking interactions, *J. Chem. Soc., Perkin Trans. 2*, 746−750. (e) Ohmichi, T., Nakano, S−i., Miyoshi, D., and Sugimoto, N. (2002) Long RNA Dangling End Has Large Energetic Contribution to Duplex Stability, *J. Am. Chem. Soc. 124*, 10367−10372 and references therein. (f) Riccelli, P. V., Mandell, K. E., and Benight, A. S. (2002) Melting studies of dangling-ended DNA hairpins: effects of end length, loop sequence and biotinylation of loop bases, *Nucleic Acids Res. 30*, 4088−4093. (g) Zuker, M. (2003) Mfold web server for nucleic acid folding and hybridization prediction, *Nucleic Acids Res. 31*, 3406−3415. (h) Limmer, S., Hofmann, H. P., Ott, G., and Sprinzl, M. (1993) The 3′-terminal end (NCCA) of tRNA determines the structure and stability of the aminoacyl acceptor stem, *Proc. Natl. Acad. Sci. U.S.A. 90*, 6199−6202. (i) Du, Z., Giedroc, D. P., and Hoffman, D. W. (1996) Structure of the Autoregulatory Pseudoknot within the Gene 32 Messenger RNA of Bacteriophages T2 and T6: A Model for a Possible Family of Structurally Related RNA Pseudoknots, *Biochemistry 35*, 4187−4198. (j) Ayer, D., and Yarus, M. (1986) The context effect does not require a fourth base pair, *Science 231*, 393−395. (k) Elbashir, S. M., Harborth, J., Lendeckel, W., Yalcin, A., Weber, K., and Tuschl, T. (2001) Formation cross-sections of singlet and triplet excitons in π-conjugated polymers, *Nature 411*, 494−497.

7. (a) Ossipov, D., Zamaratski, E., and Chattopadhyaya, J. (1998) The 5′-Purine-Pyrimidine-3′/3′-Pyrimidine-Purine-5′ stacks are more stabilizing in self-complementary DNA duplex than the 5′-Purine-Purine-3′/3′-Pyrimidine-Pyrimidine-5′ stack, *Nucleosides Nucleotides 17*, 1613−1616. (b) Maltseva, T. V., Agback, P., Repkova, M. N., Venyaminova, A. G., Ivanova, E. M., Sandström, A., Zarytova, V. F., and Chattopadhyaya, J. (1994) The solution structure of a 3′-phenazinium (Pzn) tethered DNA-RNA duplex with a dangling adenosine: r(5′GAUUGAA3′): d(5′TCAATC3′-Pzn), *Nucleic Acids Res. 22*, 5590−5599. (c) Ossipov, D., Pradeepkumar, P. I., Holmer, M., and Chattopadhyaya, J. (2001) Synthesis of $[Ru(phen)_2dppz]^{2+}$-Tethered Oligo-DNA and Studies on the Metallointercalation Mode into the DNA Duplex, *J. Am. Chem. Soc. 123*, 3551−3562. (d) Acharya, S., Acharya, P., Földesi, A., and Chattopadhyaya, J. (2002) Cross-Modulation of Physicochemical Character of Aglycones in Dinucleoside (3′→5′) Monophosphates by the Nearest Neighbor Interaction in the Stacked State, *J. Am. Chem. Soc. 124*, 13722−13730. (e) Acharya, P., Acharya, S., Földesi, A., and Chattopadhyaya, J. (2003) Tandem Electrostatic Effect from the First to the Third Aglycon in the Trimeric RNA Owing to the Nearest-Neighbor Interaction, *J. Am. Chem. Soc. 125*, 2094−2100. (f) Acharya, P., Acharya, S., Cheruku, P., Amirkhanov, N. V., Földesi, A., and Chattopadhyaya, J. (2003) Cross-Modulation of the pK_a of Nucleobases in a Single-Stranded Hexameric-RNA Due to Tandem Electrostatic Nearest-Neighbor Interactions, *J. Am. Chem. Soc. 125*, 9948−9961 and references therein. (g) Acharya, S., Földesi, A., and Chattopadhyaya, J. (2003) The pK_a of the Internucleotidic 2′-Hydroxyl Group in Diribonucleoside (3′→5′) Monophosphates, *J. Org. Chem. 68*, 1906−1910. (h) Pradeepkumar, P. I., Amirkhanov, N. V., and Chattopadhyaya, J. (2003) Antisense oligonucleotides with oxetane-constrained cytidine enhance heteroduplex stability, and elicit satisfactory RNase H response as well as showing improved resistance to both exo and endonucleases, *Org. Biomol. Chem. 1*, 81−92. (i) Zamaratski, E., Pradeepkumar, P. I., and Chattopadhyaya, J. (2001) A critical survey of the structure−function of the antisense oligo/RNA heteroduplex as substrate for RNase H, *J. Biochem. Biophys. Methods 48*, 189−208. (j) Barman, J., Acharya, P., Isaksson, J., Acharya, S., Cheruku, P., Földesi, A., and Chattopadhyaya, J. (2004) Significant pK_a Perturbation of Nucleobases Is an Intrinsic Property of the Sequence Context in DNA and RNA, *J. Am. Chem. Soc. 126*, 8674−8681.

8. (a) Narlikar, G. J., and Herschlag, D. (1997) Mechanistic Aspects of Enzymatic Catalysis: Lessons from Comparison of RNA and Protein Enzymes, *Annu. Rev. Biochem. 66*, 19−59. (b) Connell, G. J., and Yarus, M. Y. (1994) RNAs with dual specificity and dual RNAs with similar specificity *Science, 264*, 1137−1141. (c) Legault, P., and Pardi, A. (1994**)** In situ Probing of Adenine Protonation in RNA by 13C NMR, *J. Am. Chem. Soc. 116*, 8390−8391. (d) Legault, P., and Pardi, A. (1997) Unusual Dynamics and pK_a Shift at the Active Site of a Lead-Dependent Ribozyme, *J. Am. Chem. Soc. 119*, 6621−6628. (e) Ravindranathan, S., Butcher, S. E., and Feigon, J. (2000) Adenine Protonation in Domain B of the Hairpin Ribozyme, *Biochemistry 39*, 16026−16032. (f) Cai, Z., and Tinoco, I., Jr. (1996) Solution Structure of Loop A from the Hairpin Ribozyme from Tobacco Ringspot Virus Satellite, *Biochemistry 35*, 6026−6036. (g) Muth, G. W., Ortoleva-Donnelly, L., and Strobel, S. A. (2000) A Single Adenosine with a Neutral pK_a in the Ribosomal Peptidyl Transferase Center, *Science 289*, 947−950. (h) Xiong, L., Polacek, N., Sander, P., Böttger, E. C., and Mankin, A. (2001) pK_a of adenine 2451 in the ribosomal peptidyl transferase center remains elusive, *RNA, 7*, 1365−1369. (i) Drohat, A. C., and Stivers, J. T. (2000) NMR Evidence for an Unusually Low N1 pK_a for Uracil Bound to Uracil DNA Glycosylase: Implications for Catalysis, *J. Am. Chem. Soc. 122*, 1840−1841. (j) Drohat, A. C., and Stivers, J. T. (2000) *Escherichia coli* Uracil DNA Glycosylase: NMR Characterization of the Short Hydrogen Bond from His187 to Uracil O2, *Biochemistry 39*, 11865−11875. (k) Nakano, S., Chadelavada, D. M., and Bevilacqua, P. C. (2000) General Acid−Base Catalysis in the Mechanism of a Hepatitis Delta Virus Ribozyme, *Science 287*, 1493−1497. (l) Lupták, A., Ferré-D'Amaré, A. R., Zhou, K., Zilm, K. W., and Doudna, J. A. (2001) Direct pK_a Measurement of the Active-Site Cytosine in a Genomic Hepatitis Delta Virus Ribozyme, *J. Am. Chem. Soc. 123*, 8447−8452. (m) Perrotta, A. T., Shih, I., and Been, M. D. (1999) Imidazole Rescue of a Cytosine Mutation in a Self-Cleaving Ribozyme, *Science 286*, 123−126. (n) Boulard, Y., Cognet, J. A. H., Gabarro-Arpa, J., LeBret, M., Sowers, L. C., and Fazakerley, G. V. (1992) The pH dependent configurations of the C.A mispair in DNA, *Nucleic Acids Res. 20*, 1933−1941. (o) Wang, C., Gao, H., Gaffney, B. L., and Jones, R. A. (1991**)** Nitrogen-15-labeled oligodeoxynucleotides. 3. Protonation of the adenine N1 in the A·C and A·G mispairs of the duplexes {d[CG(^{15}N^1)AGAATTCCCG]}$_2$ and {d[CGGGAATTC(^{15}N^1)ACG]}$_2$, *J. Am. Chem. Soc. 113*, 5486−5488.

9. *SYBYL 6.2* (1995), Tripos, Inc., St. Louis, MO.

10. Case, D. A., Pearlman, D. A., Caldwell, J. W., Cheatham, T. E., III, Ross, W. S., Simmerling, C. L., Darden, T. A., Merz, K. M., Stanton, R. V., Cheng, A. L., Vincent, J. J., Crowley, M., Tsui, V., Radmer, R. J., Duan, Y., Pitera, J., Massova, I., Seibel, G. L., Singh, U. C., Weiner, P. K., and Kollman, P. A. (1999) *AMBER 6*, University of California, San Francisco, CA.

11. (a) Rinkel, L. J., and Altona, C. (1987) Conformational analysis of the deoxyribofuranose ring in DNA by means of sums of proton−proton coupling constants: a graphical method, *J. Biomol. Struct. Dyn. 4*, 621. (b) Thibaudeau, C., and Chattopadhyaya, J. (1999) *Stereoelectronic Effects in Nucleosides and Nucleotides and their Structural Implications* (ISBN 91-506-1351-0), Department of Bioorganic Chemistry, Uppsala University Press (jyoti@boc.uu.se), Uppsala, Sweden, and references therein.

12. Chou, S.-H., Zhu, L., Gao, Z., Cheng, J.-W., and Reid, B. R. (1996) Hairpin Loops Consisting of Single Adenine Residues Closed by Sheared A·A and G·G Pairs Formed by the DNA Triplets AAA and GAG: Solution Structure of the d(GTAC AAAGTAC) Hairpin, *J. Mol. Biol. 264*, 981−1001.

13. Kim, S.-G., Lin, L.-J., and Reid, B. R. (1992) Determination of Nucleic Acid Backbone Conformation by ^{1}H NMR, *Biochemistry 31*, 3564−3574.

14. (a) Rongata, V. K., Jones, C. R., and Gorenstein, D. G. (1990) Effect of distortions in the deoxyribose phosphate backbone conformation of duplex oligodeoxyribonucleotide dodecamers containing GT, GG, GA, AC, and GU base-pair mismatches on phosphorus-31 NMR spectra, *Biochemistry 29*, 5245−5258. (b) Chary, K. V. R., Rastogi, V. K., and Govil, G. (1993) An Efficient 2D NMR Technique HELCO for Heteronuclear [^{31}P-^{1}H] Longrange Correlation., *J. Magn. Reson. 102B*, 81−83.

15. Gorenstein, D. G. (1984) *Phosphorous-31 NMR: Principles and applications*, Academic Press, New York.
16. Lu, X.-J, and Olson, W. K. (2003) 3DNA: a software package for the analysis, rebuilding and visualization of three-dimensional nucleic acid structures, *Nucl. Acids Res. 31*, 5108−5121.
17. (a) Ditchfield, J. R. (1974) Self-consistent perturbation theory of diamagnetism I. A gauge-invariant LCAO method for N. M. R. chemical shifts, *Mol. Phys. 27*, 789−807. (b) Cheeseman, J. P., Trucks, G. W., Keith, T. A., and Frisch, M. J. (1996) A comparison of models for calculating nuclear magnetic resonance shielding tensors, *J. Chem. Phys. 104*, 5497−5509.
18. (a) Klod, S., and Kleinpeter, E. (2001) Ab initio calculation of the anisotropy effect of multiple bonds and the ring current effect of arenes−application in conformational and configurational analysis, *J. Chem. Soc., Perkin Trans. 2 10*, 1893−1898. (b) Martin, N. H., Allen, N. W., Brown, J. D., Kmiec, D. M., and Vo, L. (2003) An NMR shielding model for protons above the plane of a carbonyl group, *J. Mol. Graphics Modell. 22*, 127−131.
19. Varani, G., Aboul-ela, F., and Allain, F. (1996) NMR investigation of RNA structure, *Prog. Nucl. Magn. Reson. Spectrosc. 29*, 51−127.
20. Chan, S. I., and Nelson, J. H. (1969) Proton Magnetic Resonance Studies of Ribose Dinucleoside Monophosphates in Aqueous Solution. I. The Nature of the Base-Stacking Interaction in Adenylyl (3′→5′) adenosine, *J. Am. Chem. Soc. 91*, 168−183.
21. Isaksson, J., Zamaratski, E., Maltseva, T. V., Agback, P., Kumar, A., and Chattopadhyaya, J. (2001) The First Example of a Hoogsteen Basepaired DNA Duplex in Dynamic Equilibrium with a Watson−Crick Basepaired Duplex − A Structural (NMR), Kinetic and Thermodynamic Study, *J. Biomol. Struct. Dyn. 18*, 783−806.
22. Friedman, R. A., and Honig B. (1995) A Free Energy Analysis of Nucleic Acid Base Stacking in Aqueous Solution, *Biophys. J.* 69, 1528−1535.
23. Newcomb, L. F., and Gellman, S. H. (1994) Aromatic Stacking Interactions in Aqueous Solution: Evidence That neither Classical Hydrophobic Effects nor Dispersion Forces Are Important, *J. Am. Chem. Soc. 116*, 4993−4994.
24. Luo, R., Gilson, H. S. R., Potter, M. J., and Gilson, M. K. (2001) The Physical Basis of Nucleic Acid Base Stacking in Water, *Biophys. J. 80*, 140−148.

BI048221V